UiT
THE ARCTIC
UNIVERSITY
OF NORWAY

Department of Computer Science and Computational Engineering

Optimized cardiac simulation as a tool to understand patient specific mechanical function

—

Oscar Ofordile Odeigah

Master's Thesis in Engineering Design – June 2019

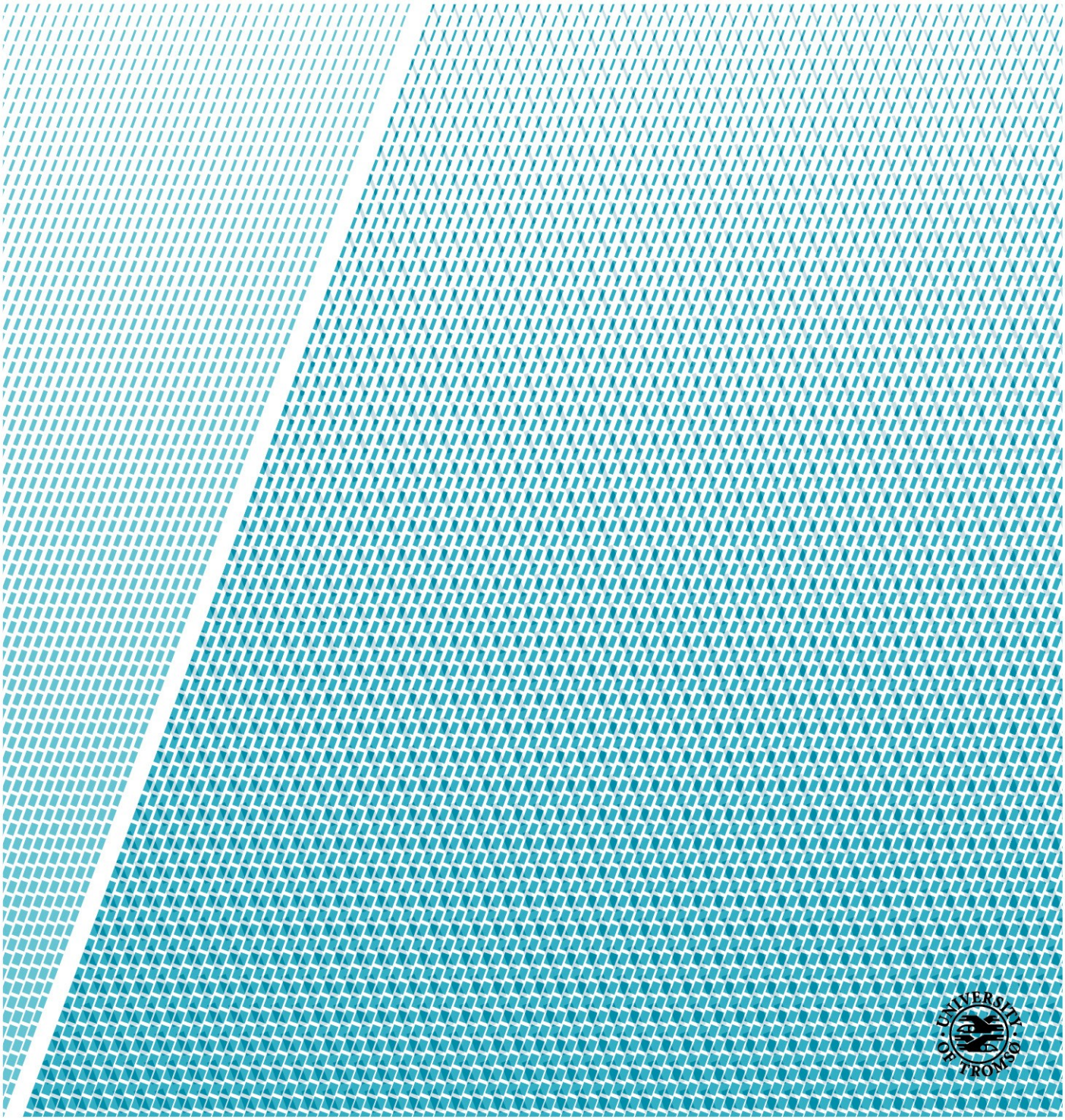

Contents

Acknowledgements iii

Abstract iv

1 Introduction 1
- 1.1 Aim of Thesis . . . 1
- 1.2 Background and Motivation . . . 2
- 1.3 Overview of the Structure and Function of the Cardiovascular System . . . 4
  - 1.3.1 Organization of the Cardiovascular System . . . 4
  - 1.3.2 Anatomy of the Heart . . . 5
  - 1.3.3 The Cardiac Cycle . . . 7
- 1.4 Basic Knowledge about Pulmonary Arterial Hypertension . . . 9

2 Review of Patient-Specific Cardiac Mechanics Models 11
- 2.1 Cardiac Geometry . . . 12
- 2.2 Myofibre Architecture . . . 13
- 2.3 Constitutive Models of the Myocardium . . . 14
- 2.4 Optimization Methods used for Patient-Specific Modelling . . . 15

3 Methods and Implementation 17
- 3.1 Data Acquisition and Processing . . . 17
  - 3.1.1 Clinical Data . . . 17
  - 3.1.2 Mesh and Fibre Generation . . . 18
  - 3.1.3 Unloaded Geometry Generation . . . 18
- 3.2 Mathematical Model . . . 19
  - 3.2.1 Force-balance Equation . . . 19
  - 3.2.2 Boundary Conditions . . . 22
  - 3.2.3 Variational Formulation . . . 24
- 3.3 Constitutive Model . . . 25
  - 3.3.1 Modelling the Passive Myocardium . . . 25

3.3.2 Modelling the Active Myocardium 26
3.4 Data Assimilation 28
3.4.1 Computing the Gradient of the Cost Function 29
3.4.2 Parameter Estimation 31
3.5 Implementation Details 31

4 Results and Discussion **33**
4.1 Matching of Simulated and Measured Data 33
4.2 Validation of Computational Models 34
4.3 Active Stress vs. Active Strain Models 36
4.3.1 Active Stress vs. Active Strain for a Simple Case of a Contracting Tissue Cube 39
4.4 Limitations and Future Directions 43

5 Conclusion **45**

APPENDIX A **56**

Acknowledgements

First of all, I would especially like to thank my supervisors Joakim Sundnes, Klas Pettersson and Samuel Wall, for providing me with very useful feedback, and directions for my thesis. Also, for always taking the time to answer any questions I had, both academically and personally.

I wish to deeply acknowledge the Computational Physiology Department at Simula Research Laboratory, for giving me the opportunity to carry out my thesis work at their facility, and for providing an outstanding working environment. In particular, a special thank you to Henrik Finsberg for the many fruitful discussions, and for guiding me in the programming aspects of my thesis; I am certainly more competent in python programming because of your help.

Finally, I would like to thank my family for always being supportive and for helping me to stay motivated during the tough periods.

Oscar Ofordile Odeigah
June, 2019

Abstract

The muscular tissue of the heart is able to contract in the absence of external load. This behaviour is stimulated by a spontaneous electrical depolarization of cardiac cells in the sinoatrial node, which spreads electrical activation through the whole heart, that triggers the synchronized mechanical contraction of the heart muscle. This phenomenon, referred to as active contraction is commonly modelled mathematically using two approaches: the active stress and the active strain approach. The active stress approach has a more physiological basis, whereas the active strain approach, is more mathematically robust and is less computationally expensive. In this thesis, we aim to investigate if both approaches (though fundamentally different in their formulations), can produce identical simulation of ventricular stress in a patient-specific bi-ventricular model. We used a computational modelling and data assimilation framework called pulse-adjoint to create the personalized models. The finite element method was used to find a numerical solution to the force-balance equation, that models heart mechanics. A gradient-based optimization method, was used to assimilate clinical data (i.e. volume and regional circumferential strain) into the computational models. To validate the models, we predicted the longitudinal and radial strains not used in the optimization. Two personalized models were created for each subject used in this study; one based on the active stress approach and the other based on the active strain approach to enable comparison between both formulations. By applying the framework using data obtained from three patients with pulmonary arterial hypertension, we were able to extract ventricular stress in the fibre, circumferential, longitudinal and radial directions. Our results show that differences exist in the stress prediction using both approaches. However, total *Cauchy* stress (in the fibre, circumferential and longitudinal directions) was simulated more closely between the two approaches, compared to the total stress in the radial direction or the deviatoric component of total stress in all four directions. We also showed that in a simple case, (simplified in terms of model geometry and myocardial fibre orientation), both approaches can produce very similar stress predictions.

1 Introduction

The muscular tissue of the heart can contract in the absence of external load. This behaviour, which is key to maintaining heart function, is commonly modelled mathematically using two approaches (the active stress and the active strain approaches), which are fundamentally different in their formulations. Here, we seek to investigate if there are differences in how both approaches simulate ventricular stress in patient-specific models of cardiovascular mechanics. Our patient-specific models were based on data from three subjects with pulmonary arterial hypertension (PAH), acquired at the National Heart Centre of Singapore, as part of an ongoing project at Simula Research Laboratory (where this thesis was conducted). From our simulations, we can conclude that both approaches simulate total stress (in the fibre, circumferential and longitudinal directions) very closely with the exception of the peak fibre stress, as was also observed in the literature [26]. However, simulation of total radial stress and the deviatoric component of stress was significantly different between both approaches.

1.1 Aim of Thesis

In this thesis, we focus on the solid mechanics aspects of the ventricular chambers of the heart and used a framework called pulse-adjoint [12] (which is based on the packages FEniCS [66] and dolfin-adjoint [24]) to create patient-specific bi-ventricular (biV) models using non-invasive data from patients with pulmonary arterial hypertension (PAH). The models are used to investigate the differences between the active-stress and active-strain approaches to modelling active contraction of the myocardium (heart muscle). The finite element method is used to find a numerical solution of the forward model (i.e. the force-balance equation) that describes the mechanics of the heart. Piecewise quadratic elements are used to discretize the displacement field and piecewise linear elements for the hydrostatic pressure field (which enforces the incompressibility constraint imposed on the myocardium). A variational data assimilation method also referred to as 4D-var is used to assimilate patient data into the computational model. This involves the min-

imization of an objective functional representing the mismatch between measured and simulated volume and regional circumferential strain, while ensuring that the forward model remained satisfied. This PDE-constrained optimisation problem is solved with a sequential quadratic programming (SQP) algorithm. The gradient of the objective functional, which is required in the algorithm, is computed automatically by solving the adjoint equation using the framework dolfin-adjoint. By minimizing the objective functional, we are able to match simulated and measured data for each of the patients used in this study. We validate the models by predicting the regional longitudinal and radial strain not used in the optimization. Finally, we extract ventricular stress results from the personalized biV models to compare stress prediction using the active stress versus the active strain approach.

This rest of this thesis is organized as follows: The remainder of this section presents a background and motivation for the work conducted in this thesis and an overview of the anatomy and physiology of the cardiac system. We conclude the section by presenting some basic knowledge about pulmonary arterial hypertension. Section 2 presents a review of existing patient-specific cardiac mechanics models and optimization methods used to fit the model to patient data. In Section 3, we present a mathematical model and constitutive relations used in modelling the mechanics of the heart. Further, we describe the method used to personalize the cardiac mechanics model and present details of the implementation in pulse-adjoint. Numerical results are presented and discussed in Section 4. We also present the limitations of these results and discuss directions for future studies in this section. Finally, in Section 5, we draw conclusions from the work conducted in this thesis.

1.2 Background and Motivation

Towards increased understanding of the causes and consequences of cardiac diseases, research in biomechanics of the heart is an active direction, motivated by the knowledge that mechanics plays a critical role in regulating cardiac function under both normal and pathological conditions [48, 57, 95]. A goal is to better understand the mechanics of the heart, to aid clinicians in making decisions and proposing treatment plans based on patient specific data; be it pharmaceutical, surgical or medical device based therapy. Computational modelling has a potential to bridge this knowledge gap and is beginning to be incorporated into clinical practice [19, 38, 63]. This method of research provides a relatively low cost framework for assessing the efficacy of therapy approaches. For

example, therapeutic parameters can be easily adjusted and assessed in multiple concurrent simulations, and also computational sensitivity studies can be easily conducted to support clinical decision making and optimise treatment planning [86].

Patient-specific modelling (PSM) came about as a result of advances in numerical methods and three-dimensional imaging techniques [49, 86, 99]. It is the development of computational models that are individualized to a patient or subject and typically involves incorporating anatomical and physiological patient data in the computational modelling workflow. This data is usually extracted non-invasively using medical imaging techniques such as magnetic resonance imaging (MRI), echocardiography and computed tomography (CT) and can also be used to validate the model [38, 50]. PSM is gaining more attention from research groups and funding agencies around the world because of its potential to improve diagnosis, optimize clinical treatment by predicting outcomes of therapies and surgical interventions, and inform the design of surgical training platforms [61, 75]. In 2015, Novo Nordisk Fond funded a consortium "MI-RISK: Risk factors for sudden cardiac death during acute myocardial infarction" with the goal being to bridge the knowledge gap between acute myocardial infarction (AMI) and sudden cardiac death (SCD) using patient-specific modelling [2]. The Research Council of Norway funds research projects on medical problems utilizing patient-specific models of heart electrophysiology and mechanics such as the *inHeart* project whose main goal is to accelerate heart failure research by facilitating the use of accurate and validated patient-specific models [1]. Furthermore, biomechanical models based on non-invasive medical imaging could provide invaluable data on the in vivo service environment where cardiovascular devices are employed and on the effect of the devices on physiologic function. In a recent study by Lee et al. [63], PSM was used to investigate the effects of the Parachute® device (developed by Cardiokinetix Inc.) on left ventricular wall stress and function. Also notable are two FDA-cleared medical devices (Heartflow® FFR_{CT}[1] and the Medtronic CardioInsight® Cardiac Mapping System[2]) which include patient-specific modelling in their workflow.

Patient-specific models have been developed representing several aspects of the cardiac system spanning disciplines such as electrophysiology, electromechanics, solid mechanics, and fluid dynamics. These models predict macroscopic phenomena such as electrical impulse propagation and active contraction of the myocardium as well as flow and pressure dynamics occurring in the ventricles, aorta and coronary arteries during each

[1] `https://www.accessdata.fda.gov/cdrh_docs/pdf15/K152733.pdf`
[2] `https://www.accessdata.fda.gov/cdrh_docs/pdf16/k162440.pdf`

cardiac cycle [38]. The mechanics of the myocardium is characterized by a passive behaviour and an active behaviour. The active response (referred to as active contraction) is unique in the sense that the muscle fibres (cardiomyocytes) can generate contractile forces by themselves; in other words, they have the ability to contract and relax in response to biochemical signals [61, 74]. Two fundamentally different approaches to model this active behaviour are available in the literature: the active stress [40] and the active strain approach [74, 95]. The active stress approach is more common and involves the additive decomposition of the stress tensor into a passive component and an active component. In other words, the activity of the cardiomyocytes is represented (mechanically) in terms of an active stress, which is to be added to the overall material stress [86]. On the other hand, the active strain formulation applies a multiplicative decomposition of the deformation gradient into a passive (elastic) deformation and active distortion [74]. Whereas the additive approach captures physiological phenomena more meaningfully, multiplicative decomposition is considered to be more mathematically robust [86].

In this thesis, the active contraction of the myocardium will be modelled using the both approaches. The aim is to determine if both formulations yield identical results, and if not, to try to understand why there are differences. Patient-specific models have been developed in a previous study [26] using the active strain formulation, as such this thesis will help to validate the results from that study. As cardiac models continue to shift from being solely research tools to potential clinical products for informing patient care, the need for robust and validated cardiac mechanics software is of key importance which serves as a motivation for the work conducted in this thesis.

1.3 Overview of the Structure and Function of the Cardiovascular System

In this section, a brief description of the structure and function of the cardiac system is presented. For a more detailed description, we refer to the books by Hoskins et al [51] and Arnold M. Katz [57] from which most of the theory in this section is taken.

1.3.1 Organization of the Cardiovascular System

The cardiovascular (or cardiac) system consists of the heart, blood vessels, and blood. It has three main functions: transport of nutrients and removal of metabolic wastes; defence and healing; thermoregulation and maintenance of fluid balance between different tissues

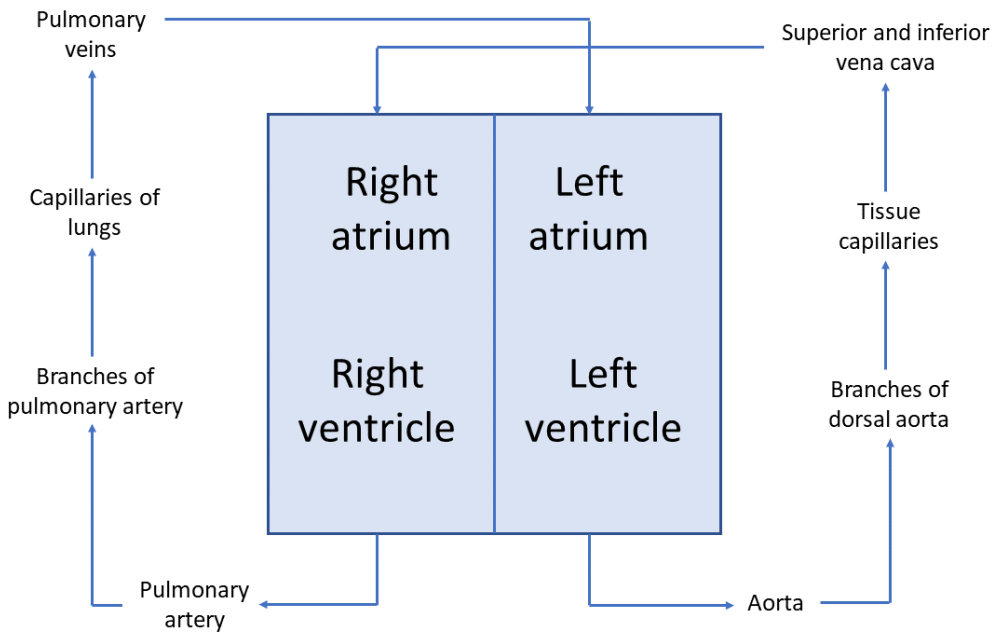

Figure 1.1: Diagram of pulmonary and systemic circulation of the cardiac system. *Reprint* from `https://en.wikipedia.org/wiki/Circulatory_system`

in the body. A flow chart of the cardiac system is shown in Figure 1.1. It comprises two sub-systems: the systemic circulation and the pulmonary circulation. The role of the heart is to pump blood through the two sub-systems. The right side of the heart supplies the pulmonary circulation which is concerned with obtaining oxygenated blood from the lungs and removing waste products of metabolism (such as carbon dioxide), while the left side supplies the systemic circulation which transports oxygenated blood to the rest of the body and also returns deoxygenated blood via the veins.

1.3.2 Anatomy of the Heart

The heart with its principal components is illustrated in Figure 1.2. On its superior end, the base of the heart is attached to the aorta, the pulmonary arteries and veins, and the vena cava, while the inferior end (the apex of the heart) rests just above the diaphragm. The base of the heart is located along the midline of the body with the apex pointing towards the left side. The heart is housed in the pericardial cavity whose walls and lining are made of a serous membrane known as the pericardium. This membrane acts to protect the heart and assist in its mechanics. It produces a serous fluid that lubricates the heart and prevents friction between the heart and its surrounding organs

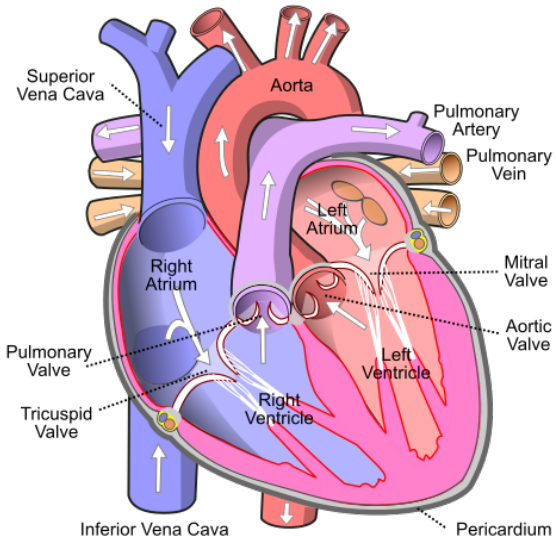

Figure 1.2: Sectioned view of the human heart. *Source*: `https://en.wikipedia.org/wiki/Heart`

and also serves to hold the heart in position while maintaining a hollow space for the heart to expand into when it is filled with blood. The heart comprises three layers of tissue: epicardium, myocardium and endocardium. The epicardium is the outermost layer of the heart and is actually the visceral layer of the pericardium. The myocardium is the middle layer and is the thickest of the three. It contains the cardiac muscle tissue and is the layer responsible for heart contractions. The endocardium is the innermost layer of the heart. It is a very smooth layer which keeps blood from sticking to the inside of the heart wall and forming blood clots.

The heart is basically a four-chambered pump with two priming chambers, the left atrium (LA) and the right atrium (RA), and two primary pumping chambers, the left ventricle (LV) and the right ventricle (RV). Its function can be divided in two main phases, referred to as the contraction (ejection) phase and the relaxation (filling) phase. The ventricles, situated in the lower part of the heart are the chambers from which blood ejects from the heart during the contraction phase. The LV ejects blood into the relatively high-pressure systemic circulation and the RV ejects blood into the low-pressure pulmonary circulation. The atria are smaller and have less muscular walls than the ventricles and are situated in the upper part of the heart. These are the chambers through which blood enters the heart during the relaxation phase. The heart valves operate as check valves thus preventing backflow of blood into the heart. During the contraction phase, the aortic and pulmonary valves are open for blood to be ejected

into the aorta and pulmonary artery respectively, while the tricuspid and mitral valves remain closed. In contrast, during the relaxation phase, the aortic and pulmonary valves remain closed while the tricuspid and mitral valves are opened for blood to fill the heart chambers via the vena cavae and the pulmonary vein, respectively.

1.3.3 The Cardiac Cycle

The cardiac cycle includes all of the events that take place during a heartbeat which approximately lasts for a second. As mentioned earlier, the heart has four chambers and at any given time during the cardiac cycle, the chambers may be found in one of two states:

- Systole - during which the cardiac muscles contract to push blood out of the chamber, and
- Diastole - during which the cardiac muscles relax to allow the chamber to fill with blood.

To start off the cycle, deoxygenated blood returning from the body enters the RA from the superior and inferior vena cava. The RA contracts and the blood is pumped through the tricuspid valve into the RV and then through the pulmonary valve into the pulmonary trunk. The pulmonary trunk carries blood to the lungs where it releases metabolic wastes and absorbs oxygen. The blood then returns to the LA via the pulmonary veins. The LA contracts to pump blood through the mitral valve into the LV. Contraction of the LV ejects blood from the heart through the aortic valve and into the aorta. From the aorta, the blood is pumped throughout the tissues of the body until it returns to the heart via the vena cavae for a repeat of the cycle.

Each heartbeat and thus the cardiac cycle begins with the spontaneous depolarisation of cells in the natural pacemaker of the heart known as the sinoatrial (SA) node, which is located in the wall of the right atrium. These cells make up about one percent of the cardiac muscle cells in the heart and set the pace for the rest of the cells. This spontaneous depolarisation causes an electrical activation to spread through the whole heart, acting as a signal to initiate and synchronise mechanical contraction of the muscle cells in the heart chambers. The cardiac muscle cells are arranged so that this contraction acts to increase the pressure in each heart chamber, leading to the synchronised opening of the valves and the pulsatile flow of blood around the circulation. Each heartbeat therefore relies on a sequence of events that include mechanical contraction, as well

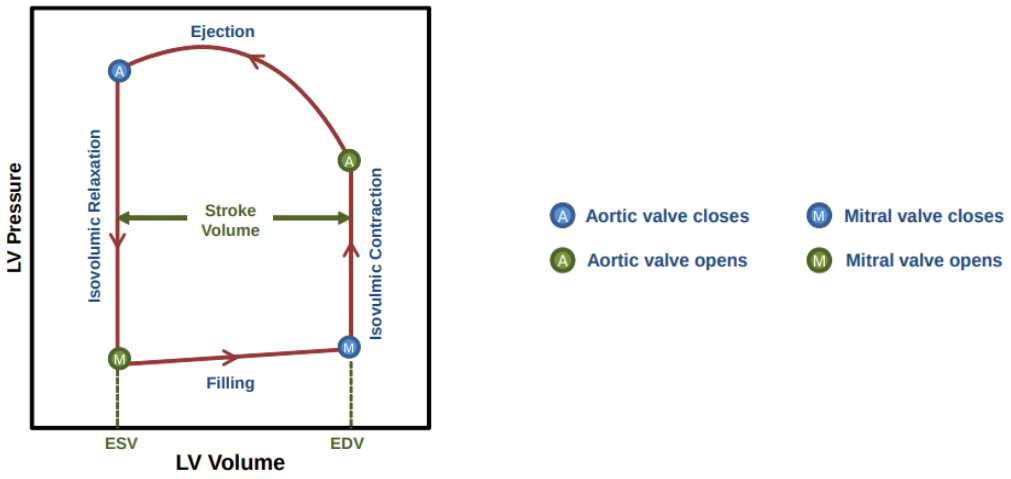

Figure 1.3: Relationship between LV pressure and LV volume during a single cardiac cycle. *Reprint* from `https://upload.wikimedia.org/wikipedia/commons/1/1c/Cardiac_Pressure_Volume_Loop.jpg`

as opening and closing of valves in the correct order. The electrical signal generated by the SA node propagates from cell to cell through the LA and RA until it reaches the atrioventricular (AV) node, another cluster of cells situated in the centre of the heart between the atria and ventricles. In a normal heart, the AV node provides the only path for the electrical signal to propagate through the atrioventricular bundle (a fibrous tissue separating atria and ventricles) to the ventricles. It acts as a gate that slows the electrical current before the signal is allowed to pass down through the LV and RV. This delay ensures that the atria are able to fully contract before the ventricles are stimulated. After passing the AV node, the electrical signal travels to the ventricles along special fibres (Purkinje fibres) embedded in the walls of the ventricles, stimulating the cardiac muscle cells to contract in a coordinated manner to pump blood out of the heart.

A common way to characterize the cardiac cycle is by means of the pressure and volume inside the individual heart chambers. A plot of pressure against volume known as a pressure-volume (PV) loop can be used to depict the changes in pressure and volume during the cardiac cycle. Figure 1.3 illustrates a typical PV-loop for the left ventricle. Proceeding anticlockwise, the loop traces the chain of events of one cardiac cycle. Systole is represented in the right and top boundaries of the loop, while the diastole is represented in the left and bottom boundaries. The bottom right corner of the loop is the mitral valve closure point, which occurs at end diastole (ED) when the pressure in the LV exceeds that of the atrium. From that point, the isovolumic contraction starts, the pressure in the LV increases at a constant volume, until the pressure exceeds that of

the aorta causing the aortic valve to open and the heart to eject blood into the body. The pressure continues to increase while the LV volume decreases as the blood is ejected rapidly into the aorta. Once the peak systolic pressure is attained, the ejection slows as both pressure and volume decrease. This continues until LV pressure becomes smaller than the aortic pressure, causing the aortic valve to close. This point is referred to as end systolic (ES) point (the top left corner in Figure 1.3) and the diastolic relaxation begins from this point. The LV first undergoes isovolumic relaxation, decreasing pressure rapidly at a constant volume, until the opening of the mitral valve when LV pressure becomes smaller than that in the atrium. The blood now flows rapidly into the LV as it completes its relaxation, this is known as the filling phase. The LV pressure and volume then increase as blood continues to flow in during the remainder of diastole, until the mitral valve closes (at ED) and the cycle repeats.

1.4 Basic Knowledge about Pulmonary Arterial Hypertension

Pulmonary arterial hypertension (PAH) is one of the five classification groups of pulmonary hypertension. It is characterized by a resting mean pulmonary arterial pressure (mPAP) of more than 25 mmHg, or an mPAP with exercise of more than 30 mmHg, with a mean pulmonary arterial wedge pressure of less than 15 mmHg [8]. It results in a progressive increase in pulmonary vascular resistance and, ultimately, leads to right ventricular failure and death. The pathogenesis of most forms of the disease is still unknown, however, three factors are thought to cause the increase in pulmonary vascular resistance: remodelling of the pulmonary arterial wall, vasoconstriction (of the pulmonary artery) and the formation of a blood clot in the pulmonary artery [23, 52]. The gold standard for diagnosis of PAH is by right heart catheterization (RHC) with the measurement of PAP, cardiac output, right atrial pressure (RAP) and pulmonary arterial wedge pressure [29]. Doppler echocardiography allows non-invasive evaluation of PAP and is increasingly being used in PAH diagnosis [8, 102]. However, the accuracy of the method is operator-dependent and it has been shown to produce an underestimation of pressures when compared with RHC [102].

Treatment options for patients with the disease have evolved over the past two decades. These treatments only help to prolong their survival and improve their quality of life, as no current therapy can cure the condition [52, 85]. We refer to the detailed review by Humbert et al. [52] of different drug therapies for treating PAH. Conven-

tional therapies include oxyen therapy (for chronic hypoxemia as a result of restricted pulmonary circulation), diuretic therapy (which reduces right ventricular preload), and oral vasodilators (to treat pulmonary artery vasoconstriction). Other therapies have a more long-term strategy such as administration of high-dose calcium-channel blockers. This therapy has been shown to produce a significant reduction in both mPAP and pulmonary vascular resistance. However, not all patients have a sustained benefit from the therapy [83, 91].

Recent advances in our understanding of the pathophysiological mechanisms that may cause PAH, have led to the development of new drug therapies and with more research and knowledge of this disease, it might soon be possible to produce a cure.

2 Review of Patient-Specific Cardiac Mechanics Models

Computational methods were first applied to compute velocity and pressure fields in idealized, generic models of vascular anatomy and physiology[27, 81, 99]. With the improvements in computing power, modelling software, availability of high-resolution medical imaging and the potential of biomechanical measurements for clinical decision-making and surgical planning, it is now possible to quantify cardiovascular mechanics in subject-specific anatomic and physiologic models [49].

Cardiac mechanics models personalized to individual patient data started gaining momentum around the year 2000 (see Figure 2.1) indexed by an exponential increase in the number of yearly publications on the topic. Since that time, many patient-specific models have been developed and utilized by different groups to investigate the development of cardiovascular disease for example in the coronary arteries [34], the carotid artery [105] and the aorta [97]. In particular, image-based models are increasingly being used to understand ventricular mechanics under pathological conditions such as myocardial infarction [3, 11], left bundle branch block [12, 25], concentric and eccentric hypertrophy [15], pulmonary arterial hypertension [113] as well as heart failure treatments [19, 63, 98]. PSM techniques have also been applied to evaluate patient-specific regional myocardial contractility and ventricular wall stresses using an optimisation approach to estimate material parameters that describe the passive myocardium [12, 25, 26].

To facilitate the discussion of existing patient-specific cardiac mechanics models, we have organized this review in terms of (1) the realistic description of the three-dimensional cardiac geometry, (2) the accurate representation of myocardial fibre architecture, and (3) the constitutive equations that characterize the material properties of the myocardium. The review also includes a discussion of some of the optimization methods used for estimating material parameters in patient-specific cardiac models.

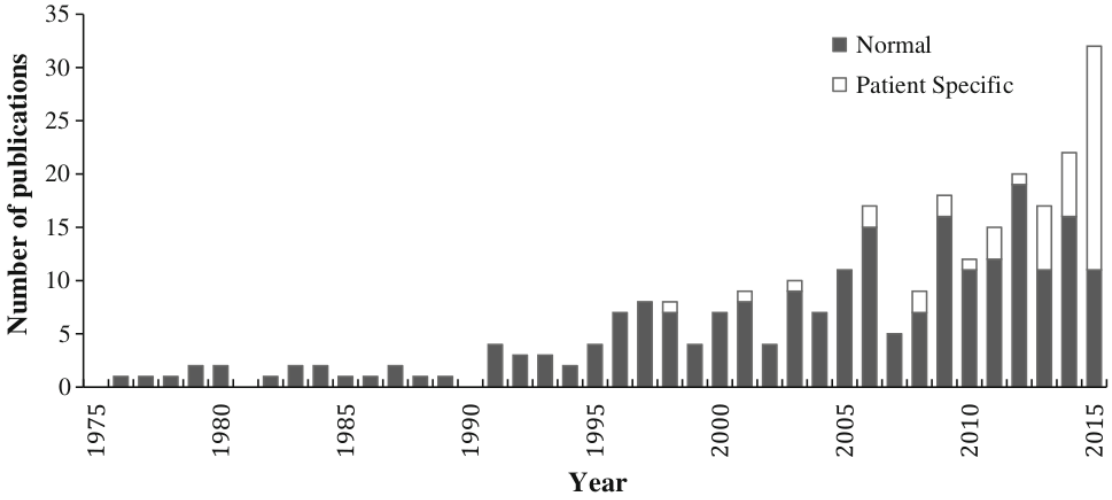

Figure 2.1: Number of yearly publications of peer-reviewed journal articles for fintie-element-based studies focusing on cardiac ventricular mechanics. *Source*: Thomson Reuters ISI Web of Knowledge and PubMed databases, January 2016

2.1 Cardiac Geometry

Until recently, simplified left ventricular geometries were used as the primary computational tool for investigating cardiac mechanics [86]. First, a spherical model was proposed for the geometry of the LV [41, 69, 112] until this was replaced by a more accurate description of the LV using a prolate ellipsoid [47, 68, 110]. The first three-dimensional patient-specific computational bi-ventricular geometry of the heart was introduced in 1968 by Okajima et al [78]. The geometry was reconstructed based on pictures taken of a heart embedded in a frozen gelatine solution. The heart was obtained at autopsy from a patient who showed no cardiac abnormality. Almost two decades later, Nielsen et al. [77] presented a realistic bi-ventricular model that was novel for its accurate geometric description and definition of myofibre orientation. The method used for reconstructing the heart geometry was similar to that used by Okajima et al. as the measurements were taken ex vivo using a canine heart. In 1972 the first use of in vivo imaging techniques for creating heart geometries was reported by Gould et al. [36]. X-ray was used to image the LV and the finite element method was used to estimate wall stress. Since then, more realistic heart geometries (derived non-invasively) have become prevalent in patient-specific computational models largely due to improvements in medical imaging techniques and computing power. Non-invasive clinical imaging techniques have become the standard procedure for anatomic model reconstruction. For example, Krams et al. [60] in 1997 used intravascular ultrasound (IVUS) to reconstruct a three-dimensional

geometry of the coronary artery to study the development of atherosclerosis. More recently, Aguado-Sierra et al. [3] used echocardiography (cardiac ultrasound) to reconstruct a bi-ventricular geometric model of a failing heart with a myocardial infarct and left ventricular bundle branch block adopting the approach developed by Nielsen et al. to create the finite element mesh from the medical images. Tang et al. [98] introduced a new model using cardiac magnetic resonance (CMR) imaging to create different zero-load diastole and systole geometries for more accurate cardiac stress/strain calculations with a potential to predict post pulmonary valve replacement surgical outcome. As the quality of imaging modalities and automatic segmentation software continue to improve, so will the accuracy of patient-specific cardiac geometries.

2.2 Myofibre Architecture

The orientation of the myofibre i.e. the spatial arrangement of ventricular myocyctes has a critical effect on cardiac mechanics as it influences both the passive and active properties of the myocardium. Indeed, myocardial fibre orientation determines the preferential electrical wave propagation and tissue contraction in the heart [22]. A recent study by Finsberg et al. [26] confirmed that finite element predictions are very sensitive to variations in fibre orientation, as such accurately representing this data is critical so that model predictions match with experimental data. Our fundamental knowledge of the myofibre architecture is based on early histological studies which found that the myocardial wall has a well-ordered distribution of fibre angles varying from about 60° at the endocardium to about -60° on the epicardium [92]. Nielsen et al. [77] in 1991 made comprehensive measurements of fibre orientation throughout the ventricular myocardium of a fixed canine heart to reveal patterns of fibre orientation that had not been previously quantified. Their results were broadly consistent with an earlier study [92], however they observed regional differences in fibre orientation on the epicardial surface. These results were used in the patient-specific model by Aguardo-Sierra et al. presented earlier.

To date no computational models have investigated cardiac function using truly individual patient-specific fibre orientation [86]. Diffusion tensor magnetic resonance imaging (DTMRI) can non-invasively provide regional information on myofibre architecture throughout the ventricular walls and is typically used to assign fibre orientation to cardiac models [3, 14, 50]. However due to challenges of performing this procedure in vivo (as it requires long acquisition and reconstruction times), the method is often

limited to a single post mortem data set from which the derived fibre orientations are mapped onto other patient-specific geometries (obtained through other imaging modalities) using for example nonlinear finite element fitting techniques [22, 86, 108]. An alternative is to use rule-based methods such as those proposed by Wong and Kuhl [111], Bayer et al. [14] or Doste et al. [22] to incorporate fibre information in cardiac computational models and this has been applied in several patient-specific models (e.g. Finsberg et al. [26]; Balaban et al. [12]). Wong and Kuhl's [111] method is capable of generating smoothly varying fibre orientations, quickly, efficiently and robustly, for both generic and patient-specific bi-ventricular models. The method proposed by Bayer at al. [14] uses a novel Laplace-Dirichlet Rule-Based (LDRB) algorithm to perform the same task as in [111] and produces results nearly indistinguishable from DTMRI-derived fibre orientations.

Recent studies have shown promising results with regards to in vivo measurement of fibre orientation using DTMRI [76, 100, 104]. In the future we should be able to investigate cardiac mechanics using wholly personalized myocardial fibre architecture.

2.3 Constitutive Models of the Myocardium

In creating a model (be it generic or patient-specific) for studying cardiac mechanics, the calculated stress distribution across the myocardial wall is dependent on the accuracy of the constitutive law chosen to characterize the material properties of the myocardium. There are several constitutive models of the passive myocardium available in the literature, including isotropic models [20], transversely isotropic models [39, 53, 54] and more recently, orthotropic models [45, 58, 87]. Several of the earlier heart mechanics models were based on linear isotropic elasticity [36, 55, 80] and proved to be too simplified and inadequate as they introduced large errors in describing the process of ejection and the transmural distribution of stresses [5]. In 2002, Dokos et al. [21] clearly showed from simple shear tests on passive ventricular myocardium (from porcine hearts) that the tissue is orthotropic having three mutually orthogonal planes with distinct material responses. Based on this study, Holzapfel and Ogden [45] developed a general framework for constitutive modelling of the passive myocardium based on invariants associated with these three directions, namely the fibre axis, the sheet axis and the sheet-normal axis. The notation and material parameters detailed by Holzapfel and Ogden have become the most widely used form of a passive material law for studying cardiac mechanics using patient-specific models [86].

To account for the active myocardium in the constitutive model, two approaches are commonly used in the literature. The first and more common approach referred to as the active stress formulation is based on the classical three-element Hill muscle model [43] and adds an active stress contribution to the overall material stress, typically oriented mainly along the local fibre orientation [40]. This formulation has been applied in many studies using patient-specific cardiac mechanics models (for e.g. Walker et al. [106]; Baillargeon et al. [9]; Usyk et al. [101]; Lee et al. [63]). The second approach, referred to as the active strain formulation, involves a multiplicative decomposition of the deformation gradient and is more mathematically robust [95]. Rossi et al. [84] used this approach for the numerical simulation of cardiac biomechanics and concluded that it is mathematically consistent and is also able to represent the main features of the phenomenon, while being less computationally expensive compared to the active stress approach. This approach has also been applied by Finsberg et al. in patient-specific models used to estimate indices of cardiac contractility and myofiber stress [25, 26]. Notably, Berberoğlu et al. [15] in 2014 used a generalization of the Hill muscle model [35] to investigate different cardiac dysfunctions (such as infarction and hypertrophy)related to the excitation-contraction coupling in the heart. This framework enabled a "best of both worlds" scenario where the advantageous features of the active stress and active strain formulations suggested in the literature were combined.

2.4 Optimization Methods used for Patient-Specific Modelling

The material parameters in the various constitutive models of the myocardium cannot be extracted *in vivo*. As such, in patient-specific models, these parameters are estimated using a method that fits the output of the model to patient data. In other words, a set of material parameters are selected and tuned until the error between the simulated output and measured data is below a set tolerance limit. This is typically achieved by defining a so-called objective function which represents the mismatch between simulated and measured data, such that a minimization of this function serves to bring the simulated data close to the measured data. Several optimization algorithms have been used in the literature to solve such parameter estimation problems such as *sequential quadratic programming* (SQP) algorithm [7, 10, 26, 108], *genetic* algorithm [70, 71, 73], BOBYQA (Bound Optimization BY Quadratic Approximation) algorithm [32, 88] and *parameter sweeps* method [114]. The SQP algorithm is a gradient-based optimization technique

that uses the derivative of the objective function (i.e. the functional gradient) to find a search direction that leads to a local minimum of the function. This algorithm uses relatively few iterations to converge to a minimum but has a disadvantage in that they converge to a local minimum which might not be the optimal solution in the case of a function with several local minima. One way to circumvent this challenge is to apply a multi-start optimization method where many optimizations are run from randomly chosen initial parameter points and the parameter set that gives the best fit is chosen as the optimal set. This method was used by Balaban et al. [10] to estimate cardiac hyperelastic material parameters from shear data. Furthermore, optimization methods which require gradient information are not suited to functions that are non-differentiable. For such functions, the BOBYQA algorithm which is a derivative-free optimization technique developed by Michael J.D. Powell in 2009 [82] is more practical and was used by Genet et al. [32] to estimate passive material parameters. They were able to predict circumferential and longitudinal strains to within 6 % of measured values using this method. *Genetic* algorithms mostly converge towards a global minimum of the function and were found to be a robust method for estimating myocardial material parameters in a study by Nair et al. [73]. Using a realistic 3D heart model, they were able to achieve optimized material parameters to within 5 % of the true values. Roch Molléro et al. [71] also used a genetic algorithm called CMA-ES (which stands for Co-variance Matrix Adaptation Evolution Strategy) in their parameter estimation framework for cardiac models. This algorithm is known to produce very good results on problems involving a large parameter space [31, 42]. However, some of the drawbacks associated with global optimization algorithms (such as the genetic algorithm) are that they are computationally expensive as they typically require a lot of functional evaluations, and for even the most basic variations of the algorithm there are several problem-dependent parameters that need to be tuned by the user [103]. In the *parameter sweeps* method, a range of values for each parameter is selected, and simulations are run with all possible combinations of these values from which the optimal set of parameters is chosen. This exhaustive method was utilized by Xi et al. [114] to fit a passive mechanics model to patient data. An obvious drawback with this method is that the computational cost increases with the number of model parameters. Also, as some parameters will have much less effect on the objective function, this will lead to a number of redundant simulations. However, if the importance of each parameters is known, then this can inform the number of values picked for each parameter, thus reducing the required number of simulations to achieve an optimized parameter set.

3 Methods and Implementation

In this section, we present the methods used for patient specific modeling in this thesis. Except otherwise stated, the methodology is based on the work by Finsberg et al. [26]. The medical data acquisition, biV mesh and myocardial fibre generation were not carried out as part of this thesis. The medical data was acquired at the National Heart Centre of Singapore with written informed consent obtained from all participants, while the biV mesh and myocardial fibre generation was done by the Computational Physiology Department[1] at Simula Research Laboratory (where this thesis was conducted). However, the methods for carrying out these tasks are described here for completeness.

3.1 Data Acquisition and Processing

Here, we will describe the methods used to extract the clinical patient data, to generate the bi-ventricular mesh from medical images and to assign myocardial fibre orientation to the models. We also describe the method used in this thesis to derive the reference geometry relevant for the simulations.

3.1.1 Clinical Data

Data from four PAH patients (referred to here as MR011, MR015, MR016 and MR019) who underwent both cardiac magenetic resonance (MR) imaging and right heart catheterization (RHC) was used in this thesis. A 3T Philips scanner was used to acquire cine MR images from the patients in multi-planar short- and long-axis views. Three-dimensional bi-ventricular geometries were then reconstructed from the cine MR images and partitioned into 3 regions comprising the left ventricular free wall (LVFW), right ventricular free wall (RVFW) and interventricular septum (SEPT) as shown in Figure 3.1a. RHC was used to acquire left and right ventricular pressure while cavity volumes of the LV and RV were measured at different time frames within a cardiac cycle using the MR-

[1] `https://www.simula.no/research/projects/department-computational-physiology`

reconstructed bi-ventricular geometries. These pressure and volume data were synchronized and used to reconstruct the LV and RV pressure-volume loops for the patients.

Regional circumferential and longitudinal strain were estimated from the cine images using a hyperelastic warping method described in [116]. Normal strains in the circumferential and longitudinal directions at the LVFW, RVFW and SEPT were computed from the displacement field using the end-diastole as the reference configuration. Note that the circumferential and longitudinal directions in the bi-ventricular model were assigned using a Laplace-Dirichlet-Rule-Based algorithm as described in [14].

3.1.2 Mesh and Fibre Generation

For each patient, three-dimensional finite element meshes (see Figure 3.1b) were generated in the volume enclosed by the endocardial and epicardial surfaces using GMSH [33]. These surfaces were cut by a least squares fitting plane fitted to the basal points of the surfaces, and then the plane was adjusted so that the cavity volume in the mesh was within 1 mL of the measured volume. Points on the epi- and endocardial surfaces above the cutting plane were discarded.

The myocardial fibre orientation, denoted by $\mathbf{f}_0$, were assigned using a rule-based algorithm described in [14], with the helix fibre angles set to 60° on the endocardium and rotated clockwise throughout the ventricular wall to -60° on the epicardium. A representation of the myocardial fibres is shown in Figure 3.1c.

3.1.3 Unloaded Geometry Generation

In principle, the patient-specific geometry reconstructed from medical images is not stress-free because the observed images represent a configuration of the heart already stressed by in vivo conditions such as blood pressure. Hence, we need to estimate the unloaded (zero-pressure) geometry which will revert back to the original reconstructed geometry (during the simulation). Several computational strategies exist to achieve this based on for example inverse design analysis [30], a modified updated Lagrangian formulation [30, 37] and a backward displacement method [16, 89]. Some studies have instead used images extracted at atrial systole [11, 12] or early ventricular diastole [113, 114] to represent the unloaded geometry as the LV and RV pressures can be considered close to the minimum at these points. As part of the work carried out in this thesis, an estimate of the unloaded geometry was found by applying the backward displacement method described in [16]. Note that for bi-ventricular geometries, this method might

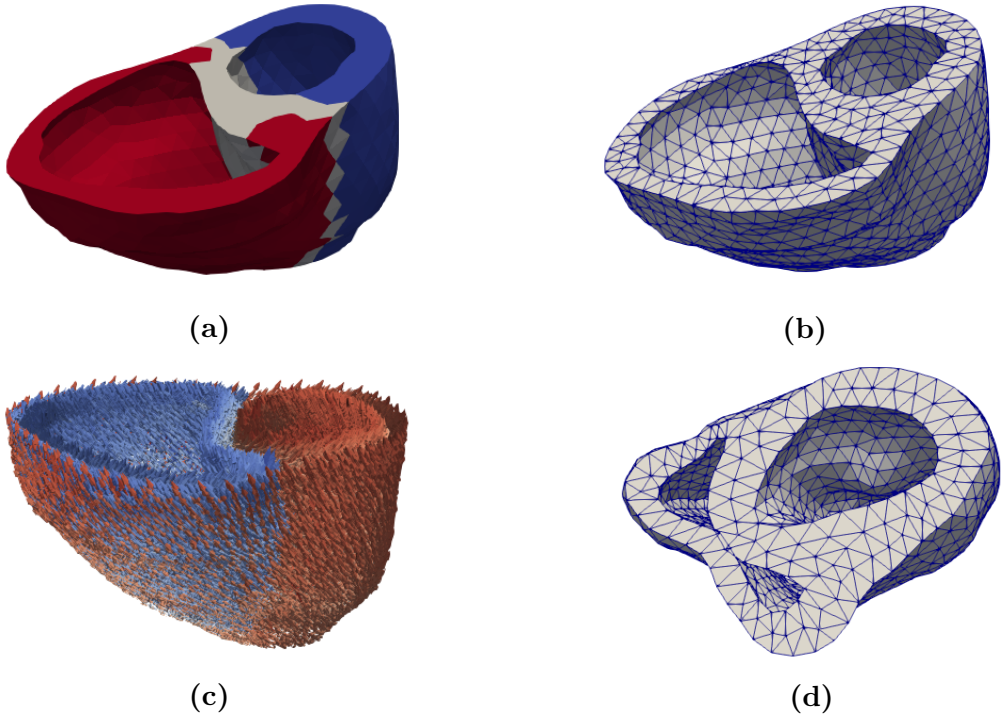

Figure 3.1: (a) Partition of regions: RVFW (red); SEPT (gray); LVFW (blue). **(b)** Finite element mesh model. **(c)** Myocardial fibre orientation with a transmural variation of 60° (endo) to −60° (epi) for the bi-ventricular model. **(d)** Collapsed RVFW as a result of failed unloading, which can occur if the myocardial tissue is soft and the pressure in the RV is high.

fail to converge, particularly if the tissue is soft and the pressure in the right ventricle is high leading to buckling of the RVFW (see Figure 3.1d). This was observed with one of the subjects (MR015) used in this thesis.

3.2 Mathematical Model

In this section, we will introduce the concepts of continuum mechanics necessary to model the mechanics of the heart. For a detailed description of the theory and derivations of the equations we refer to books by Gerhard Holzapfel [44] and Stuart S. Antman [4].

3.2.1 Force-balance Equation

We represent the heart as a continuum body in $\mathbb{R}^3$. We denote the current configuration of the heart by $\boldsymbol{\omega}$, and the reference configuration by $\boldsymbol{\Omega}$. We use $\mathbf{x}$ to denote the current position of a material particle in $\boldsymbol{\omega}$ that was originally placed at $\mathbf{X}$ in $\boldsymbol{\Omega}$. The

motion of the continuum body is defined using the smooth one-to-one map $\varphi : \mathbf{\Omega} \to \omega$, $\varphi(\mathbf{X}) = \mathbf{X} + \mathbf{u}(\mathbf{X})$ where $\mathbf{u}$ denotes the displacement vector $\mathbf{u} = \mathbf{x} - \mathbf{X}$ which relates postions in the reference configuration to positions in the current configuration.

We now define some other quantities relevant to modelling cardiac mechanics. The *deformation gradient* is a second order strain tensor which maps vectors in the reference configuration to vectors in the current configuration and is represented as

$$\mathbf{F} = \operatorname{Grad} \mathbf{x}. \tag{3.1}$$

Since $\mathbf{x} = \mathbf{u} + \mathbf{X}$, we have that

$$\mathbf{F} = \operatorname{Grad} \mathbf{u} + \operatorname{Grad} \mathbf{X} = \operatorname{Grad} \mathbf{u} + \mathbf{I}, \tag{3.2}$$

where $\mathbf{I}$ is the identity tensor. From this, we define the volume map as the determinant of the *deformation gradient* such that an infinitesimal volume element $\mathrm{d}V$ in $\mathbf{\Omega}$ is related to an infinitesimal volume element $\mathrm{d}v$ in ω as below

$$\mathrm{d}v = \det(\mathbf{F})\, \mathrm{d}V. \tag{3.3}$$

Also associated with the *deformation gradient*, are the *right Cauchy-Green* deformation tensor, $\mathbf{C} = \mathbf{F}^\top \mathbf{F}$, and the *left Cauchy-Green* deformation tensor, $\mathbf{B} = \mathbf{F}\mathbf{F}^\top$. Another useful expression for strain relevant to cardiac mechanics is the *Green-Lagrange* strain tensor defined as $\mathbf{E} = \frac{\mathbf{1}}{\mathbf{2}}(\mathbf{C} - \mathbf{I})$.

The force-balance equation for the mechanics of the heart is based on the principle of conservation of linear momentum which states that the change in linear momentum of a body equals the total applied force acting on the body. For a continuum body with constant mass density, ρ this implies that

$$\int_\omega \rho \dot{\mathbf{v}}\, \mathrm{d}v = \mathbf{f}, \qquad \mathbf{f} = \int_{\partial\omega} \mathbf{t}\, \mathrm{d}s + \int_\omega \rho \mathbf{b}\, \mathrm{d}v, \tag{3.4}$$

where $\dot{\mathbf{v}}$ is the spatial velocity field and the total applied force $\mathbf{f}$ (given as the sum of a volume and surface integral) comprises a tractive force, $\mathbf{t}$ and a body force, $\mathbf{b}$.
By *Cauchy's* theorem, the tractive force vector, depends linearly on a unit normal $\mathbf{n}$; that is, there exists a second order tensor σ (called the *Cauchy* stress tensor) such that $\mathbf{t} = \sigma\mathbf{n}$. This implies that

$$\int_{\partial\omega} \mathbf{t}\, \mathrm{d}s = \int_{\partial\omega} \sigma\mathbf{n}\, \mathrm{d}s,$$

and using the divergence theorem we get

$$\int_{\partial\omega} \mathbf{t}\,\mathrm{d}s = \int_{\partial\omega} \sigma\mathbf{n}\,\mathrm{d}s = \int_{\omega} \boldsymbol{\nabla}\cdot\sigma\,\mathrm{d}v. \tag{3.5}$$

By combining (3.4) and (3.5) we get

$$\int_{\omega} \rho\dot{\mathbf{v}}\,\mathrm{d}v = \int_{\omega} \boldsymbol{\nabla}\cdot\sigma\,\mathrm{d}v + \int_{\omega} \rho\mathbf{b}\,\mathrm{d}v,$$

from which we arrive at *Cauchy's* equation of motion

$$\boldsymbol{\nabla}\cdot\sigma + \rho\mathbf{b} = \rho\dot{\mathbf{v}}. \tag{3.6}$$

The contributions from the body force, $\mathbf{b}$, and the inertial term, $\rho\dot{\mathbf{v}}$ can be considered negligible compared to the stress term [72, 96], thus we have the force balance equation as

$$\boldsymbol{\nabla}\cdot\sigma = \mathbf{0}. \tag{3.7}$$

Note that (3.7) is formulated in the current configuration as the *Cauchy* stress tensor relates forces to areas in the current configuration. An equivalent formulation in the reference configuration is

$$\boldsymbol{\nabla}\cdot\mathbf{P} = \mathbf{0}, \tag{3.8}$$

where $\mathbf{P}$ is the first *Piola-Kirchhoff* stress tensor and is related to σ via the expression,

$$\mathbf{P} = J\sigma\mathbf{F}^{-\top}, \qquad \text{or} \qquad \sigma = J^{-1}\mathbf{P}\mathbf{F}^{\top}, \tag{3.9}$$

with $J = \det(\mathbf{F})$. In this thesis, the myocardium is modelled as a hyperelastic material which implies that the stress-strain relationship is derived from a strain energy density function, $\boldsymbol{\Psi}$ and the first *Piola-Kirchhoff* stress tensor is given as

$$\mathbf{P} = \frac{\partial\boldsymbol{\Psi}(\mathbf{F})}{\partial\mathbf{F}}. \tag{3.10}$$

The actual strain energy density function used (in the constitutive model) in this thesis will be presented in Section 3.3.

A common assumption in cardiac mechanics modelling, which has also been applied in this thesis, is to model the myocardium as an incompressible material, implying that the volume remains constant during deformations. This means that a constraint is

placed on the volume map (see Equation (3.3)) such that

$$J = \det(\mathbf{F}) = 1, \quad \text{or} \quad J - 1 = 0. \tag{3.11}$$

Thus, to ensure incompressibility of the hyperelastic myocardium, the strain energy density function is modified to the isochoric form

$$\mathbf{\Psi} = \mathbf{\Psi}(\mathbf{F}) + p(J-1), \tag{3.12}$$

where the hydrostatic pressure p serves as a *Lagrange multiplier* to enforce the incompressibility constraint. The first *Piola-Kirchhoff* stress tensor then becomes

$$\mathbf{P} = \frac{\partial \mathbf{\Psi}(\mathbf{F})}{\partial \mathbf{F}} - Jp\mathbf{F}^{-\top}, \tag{3.13}$$

and from (3.9) we derive the *Cauchy* stress tensor as

$$\sigma = J^{-1}\frac{\partial \mathbf{\Psi}(\mathbf{F})}{\partial \mathbf{F}}\mathbf{F}^{\top} - p\mathbf{I}. \tag{3.14}$$

3.2.2 Boundary Conditions

Boundary conditions are required to solve differential equations such as the force-balance equation (3.8) and when imposed on a model, they should mimic, as close as possible, what is observed in reality. Different approaches have been proposed to constrain biventricular models in the literature [28, 79, 107, 109]. In this thesis, a Neumann boundary condition was used for the endocardium representing the endocardial blood pressure. For the left and right ventricles we have

$$\sigma\mathbf{n} = -p_{\text{lv}}\mathbf{n},\ \forall \mathbf{x} \in \delta\omega_{\text{endo,LV}}, \qquad \text{and} \qquad \sigma\mathbf{n} = -p_{\text{rv}}\mathbf{n},\ \forall \mathbf{x} \in \delta\omega_{\text{endo,RV}}, \tag{3.15}$$

where $\delta\omega_{\text{endo,LV}}$ and $\delta\omega_{\text{endo,RV}}$ represent the left and right endocardial domains respectively, p_{lv} and p_{rv} the blood pressure in the LV and RV respectively, and $\mathbf{n}$ is the unit outward facing boundary normal. This condition is imposed on the current configuration. To impose it on the reference configuration we used the transformation in (3.9) to obtain

$$\begin{aligned} &\mathbf{PN} = -p_{\text{lv}}J\mathbf{F}^{-\top}\mathbf{N},\ \forall \mathbf{X} \in \delta\mathbf{\Omega}_{\text{endo,LV}}, \quad \text{and} \\ &\mathbf{PN} = -p_{\text{rv}}J\mathbf{F}^{-\top}\mathbf{N},\ \forall \mathbf{X} \in \delta\mathbf{\Omega}_{\text{endo,RV}}. \end{aligned} \tag{3.16}$$

The ventricular base was fixed using a Dirichlet boundary condition,

$$u_1 = 0,\ \forall \mathbf{X} \in \delta\mathbf{\Omega}_{\text{base}}, \tag{3.17}$$

where u_1 is the longitudinal component of the displacement field $\mathbf{u} = (u_1, u_2, u_3)$. Finally, the epicardial surface of the bi-ventricular geometry was constrained using a Robin type boundary condition

$$\mathbf{PN} + k\mathbf{u} = 0,\ \forall \mathbf{X} \in \delta\mathbf{\Omega}_{\text{epi}}, \tag{3.18}$$

where $\mathbf{PN} = -p_{\text{epi}} J\mathbf{F}^{-\top}.\mathbf{N},\ \forall \mathbf{X} \in \delta\mathbf{\Omega}_{\text{epi}}$ and k is the stiffness of a spring that limits the movement of the epicardium such that $k = 0$ and $k \to \infty$ represent a free and fixed boundary respectively. A linear spring stiffness $k = 0.5\,\text{kPa/cm}$ was used in this thesis based on a previous study [113]. Note that an often used simplification which was also applied in this thesis is to set the epicardial pressure p_{epi} to zero [93, 107]. A bi-ventricular geometry illustrating the different boundary conditions applied in this thesis is presented in Figure 3.2.

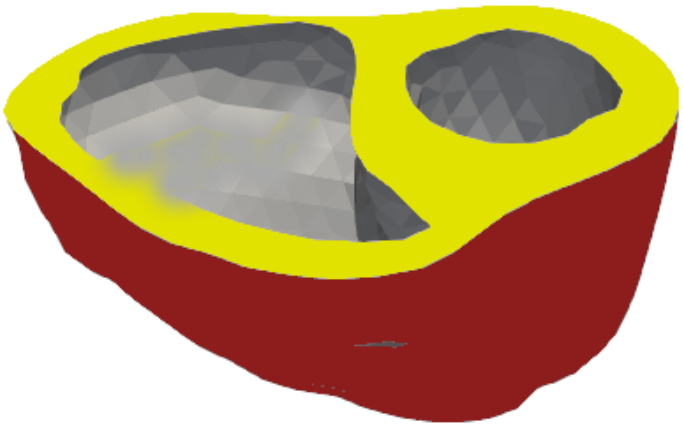

Figure 3.2: Boundary conditions on the biV model: Dirichlet BC (yellow); Neumann BC (gray); Robin BC (red).

3.2.3 Variational Formulation

Considering the myocardium as an incompressible, hyperelastic material we have the strong form of the force-balance equation in the Lagrangian formulation

$$\begin{aligned} \boldsymbol{\nabla} \cdot \mathbf{P} &= \mathbf{0} \\ J - 1 &= 0, \end{aligned} \tag{3.19}$$

with boundary conditions as defined in Section 3.2.2. To find a numerical solution to (3.19) using the finite element method, we first need to express it in a variational (weak) form. To achieve this, we utilized the *principle of stationary potential energy* which states that a physical system is at equilibrium when the total potential energy is minimized, and any infinitesimal variation from this state involves no change in energy. For an incompressible, hyperelastic material the total potential energy, $\boldsymbol{\Pi}$ in the system is given as

$$\boldsymbol{\Pi}(\mathbf{u}, p) = \boldsymbol{\Pi}_{\text{int}}(\mathbf{u}, p) + \boldsymbol{\Pi}_{\text{ext}}(\mathbf{u}), \tag{3.20}$$

$$\boldsymbol{\Pi}_{\text{int}}(\mathbf{u}, p) = \int_{\Omega} [p(J-1) + \boldsymbol{\Psi}(\mathbf{F})] \, \mathrm{d}V, \tag{3.21}$$

$$\boldsymbol{\Pi}_{\text{ext}}(\mathbf{u}) = -\int_{\Omega} \mathbf{B}.\mathbf{u} \, \mathrm{d}V - \int_{\partial\Omega_N} \mathbf{T}\mathbf{u} \, \mathrm{d}S, \tag{3.22}$$

where $\boldsymbol{\Pi}_{\text{int}}$ represents the internal (strain) energy stored in the deformed body and $\boldsymbol{\Pi}_{\text{ext}}$ represents the external potential energy associated with external forces. According to the *principle of stationary potential energy* we find the stationary conditions with respect to $\mathbf{u}$ and p as

$$D_{\delta\mathbf{u}}\boldsymbol{\Pi}(\mathbf{u}, p) = 0, \qquad \text{and} \qquad D_{\delta p}\boldsymbol{\Pi}(\mathbf{u}, p) = 0. \tag{3.23}$$

That is we compute and set to zero the directional derivatives of $\boldsymbol{\Pi}$ with respect to a virtual displacement field $\delta\mathbf{u}$ and a virtual hydrostatic pressure field δp. With reference to (3.23) we substitute (3.21) and (3.22) into (3.20) and obtain the weak forms (derivations have been omitted)

$$D_{\delta\mathbf{u}}\boldsymbol{\Pi}(\mathbf{u}, p) = \int_{\Omega} [pJ\mathbf{F}^{-\top} + \mathbf{P}] : \boldsymbol{\nabla}\delta\mathbf{u} \, \mathrm{d}V + D_{\delta\mathbf{u}}\boldsymbol{\Pi}_{\text{ext}} = 0, \tag{3.24}$$

in the direction of the virtual displacement field, and

$$D_{\delta p}\boldsymbol{\Pi}(\mathbf{u}, p) = \int_{\Omega} (J-1)\delta p \, \mathrm{d}V = 0, \tag{3.25}$$

in the direction of the virtual hydrostatic pressure field. The second term in (3.24) is associated with the external forces applied as boundary conditions on the model, that is

$$D_{\delta\mathbf{u}}\mathbf{\Pi}_{\text{ext}} = \int_{\delta\Omega_{\text{endo,LV}}} p_{\text{lv}} J\mathbf{F}^{-\top}\mathbf{N}\delta\mathbf{u}\,\mathrm{d}S + \int_{\delta\Omega_{\text{endo,RV}}} p_{\text{rv}} J\mathbf{F}^{-\top}\mathbf{N}\delta\mathbf{u}\,\mathrm{d}S + \int_{\delta\Omega_{\text{epi}}} k\mathbf{u}\delta\mathbf{u}\,\mathrm{d}S. \tag{3.26}$$

The variational equations (3.24) and (3.25) provide the fundamental basis for the finite element implementation and are commonly referred to as the *Euler-Lagrange* equations. If we denote V and Q as two suitable Hilbert spaces for the displacement $\mathbf{u}$ and the hydrostatic pressure p respectively, then the variation formulation reads:
Find $(\mathbf{u}, p) \in V \times Q$ *such that* $\forall(\delta\mathbf{u}, \delta p) \in V \times Q$,

$$\begin{aligned} D_{\delta\mathbf{u}}\mathbf{\Pi}(\mathbf{u}, p) &= 0, \quad \text{and} \\ D_{\delta p}\mathbf{\Pi}(\mathbf{u}, p) &= 0. \end{aligned} \tag{3.27}$$

Discretization of the Force Balance Equations

In deriving the variational form in Section 3.2.3, we utilized a two-field variational principle because finite element analysis of problems associated with constraint conditions (such as the incompressibility constraint imposed in this thesis) experience significant numerical difficulties if we choose to discretize over only one field i.e. the displacement field. These difficulties, referred to as *locking phenomena*, arise from the over-stiffening of the system causing instability in the numerical solution [44]. To eliminate this, we discretize the displacement field and the hydrostatic pressure field independently using a mixed finite elements method. The elements used in this thesis are the Taylor-Hood mixed finite elements [46]; that is, a piecewise quadratic discretization of the displacement field and a piecewise linear discretization of the hydrostatic pressure field. These mixed elements satisfy the discrete inf-sup condition [62] which is a requirement for stability of the numerical solution.

3.3 Constitutive Model

3.3.1 Modelling the Passive Myocardium

In this thesis, we will use a constitutive law proposed by Holzapfel and Ogden [45] to model the passive myocardium. This law takes into account the orthotropic nature of the myocardial tissue that is the presence of three mutually orthogonal directions of

alignment of cardiac cells namely the fiber axis, $\mathbf{f}_0$, sheet axis, $\mathbf{s}_0$, and sheet-normal axis, $\mathbf{n}_0$. The invariant-based nature of this law also makes it independent of the frame of reference. The orthotropic model proposed by Holzapfel and Ogden has the form

$$\Psi = \frac{a}{2b}e^{b(I_1-3)} + \frac{a_\mathrm{f}}{2b_\mathrm{f}}[e^{b_\mathrm{f}(I_{4\mathbf{f}_0}-1)^2} - 1] + \frac{a_\mathrm{s}}{2b_\mathrm{s}}[e^{b_\mathrm{s}(I_{4\mathbf{s}_0}-1)^2} - 1] + \frac{a_\mathrm{fs}}{2b_\mathrm{fs}}[e^{b_\mathrm{fs}I^2_{8\mathbf{f}_0\mathbf{s}_0}} - 1], \quad (3.28)$$

where a, b, a_f, a_s, b_f, b_s, a_fs and b_fs are positive material parameters, with the a parameters having dimensions of stress and the b parameters dimensionless. We define the invariants I_1, $I_{4\mathbf{f}_0}$, $I_{4\mathbf{s}_0}$ and $I_{8\mathbf{f}_0\mathbf{s}_0}$ as

$$I_1 = \mathrm{tr}(\mathbf{C}), \qquad I_{4\mathbf{f}_0} = \mathbf{f}_0.(\mathbf{C}\mathbf{f}_0), \qquad I_{4\mathbf{s}_0} = \mathbf{s}_0.(\mathbf{C}\mathbf{s}_0), \qquad I_{8\mathbf{f}_0\mathbf{s}_0} = \mathbf{s}_0.(\mathbf{C}\mathbf{f}_0), \quad (3.29)$$

with $\mathbf{f}_0$ and $\mathbf{s}_0$ being unit vectors aligned with the fiber and sheet directions respectively. Since the myocardium can be considered to have a preferred direction which is the fiber axis $\mathbf{f}_0$, we used a transversely isotropic version of (3.28) in this thesis to reduce the number of model parameters. To achieve this, we set $a_s = b_s = a_{fs} = b_{fs} = 0$ and get the strain energy density function on the form

$$\Psi = \frac{a}{2b}e^{b(I_1-3)} + \frac{a_\mathrm{f}}{2b_\mathrm{f}}[e^{b_\mathrm{f}(I_{4\mathbf{f}_0}-1)^2} - 1], \quad (3.30)$$

which yields the *Cauchy* stress tensor (see [45] for derivation),

$$\sigma = a\, e^{b(I_1-3)}\mathbf{B} + 2a_\mathrm{f}(I_{4\mathrm{f}} - 1)e^{b_\mathrm{f}(I_{4\mathrm{f}}-1)^2}\mathbf{f}\otimes\mathbf{f} - p\mathbf{I}, \quad (3.31)$$

where $\mathbf{B}$ is the left *Cauchy-Green* tensor defined earlier, $\mathbf{f} = \mathbf{F}\mathbf{f}_0$ and $\otimes$ signifies the outer product.

3.3.2 Modelling the Active Myocardium

As stated in Section 1 the myocardium exhibits a non-standard continuum mechanics behaviour as the muscle fibres can generate contractile forces by themselves (in response to biochemical signals) without the application of external loads. There are two common approaches used in cardiac mechanics to mathematically describe this behaviour; the active stress and the active strain formulation. In this thesis, the active stress formulation will be used. For a detailed description of the formulation, we refer to [40]. In this approach, the total *Cauchy* stress σ is decomposed additively into a passive contribution

σ_p and an active contribution σ_a (termed as the active stress),

$$\sigma = \sigma_p + \sigma_a. \tag{3.32}$$

The passive contribution is based on the material model in Section 3.3.1 and is calculated using (3.31) while the active stress is given by

$$\sigma_a = \sigma_{ff}\mathbf{f} \otimes \mathbf{f} + \sigma_{ss}\mathbf{s} \otimes \mathbf{s} + \sigma_{nn}\mathbf{n} \otimes \mathbf{n}, \tag{3.33}$$

where σ_{ff}, σ_{ss}, and σ_{nn} are the active stress in the fiber, sheet and sheet-normal directions respectively, $\mathbf{s} = \mathbf{F}\mathbf{s}_0$ and $\mathbf{n} = \mathbf{F}\mathbf{n}_0$. If we consider the active stress in the transverse directions ($\sigma_s s$ and $\sigma_n n$) to be non-negligible (which is supported by experimental evidence [65]), then we can assume a uniform transverse activation such that (3.33) can be written as

$$\sigma_a = T_a[\mathbf{f} \otimes \mathbf{f} + \eta(\mathbf{s} \otimes \mathbf{s} + \mathbf{n} \otimes \mathbf{n})], \tag{3.34}$$

where η represents the amount of transverse activation and T_a is the magnitude of the active stress such that when $\eta = 0$, the active tension acts purely in the fiber direction and (3.34) reduces to $\sigma_a = T_a\mathbf{f} \otimes \mathbf{f}$. We set $\eta = 0.2$ in this thesis based on a previous study [94]. Note that this simplification of (3.33) is possible as we consider the myocardium as a transversely isotropic material, implying that the material response along the transverse directions is the same.

For completeness we present the formulation for the active strain approach. For a detailed description of the formulation, we refer to [95] and [74]. In this approach, a multiplicative decomposition of the *deformation gradient* is adopted, that is,

$$\mathbf{F} = \mathbf{F}_e\mathbf{F}_a, \tag{3.35}$$

where $\mathbf{F}_e$ is the *elastic* deformation, $\mathbf{F}_a$ is the *active* deformation and $\mathbf{F}$ is referred to as the *visible* deformation. The elastic deformation is defined as the difference between the active and the visible one

$$\mathbf{F}_e = \mathbf{F}\mathbf{F}_a^{-1}, \tag{3.36}$$

while the active deformation for a transversely isotropic material with an active response has the form

$$\mathbf{F}_a = (1-\gamma)\mathbf{f}_0 \otimes \mathbf{f}_0 + \frac{1}{\sqrt{1-\gamma}}(\mathbf{I} - \mathbf{f}_0 \otimes \mathbf{f}_0), \tag{3.37}$$

where γ is associated with the relative active shortening along the muscle fibers. Note

that the constraint $\det(\mathbf{F}_a) = 1$ is considered in the formulation so that the active deformation is also volume preserving.

3.4 Data Assimilation

In order to incorporate patient data into the cardiac mechanics model a variational data assimilation approach was used which is based on minimizing an objective functional that represents the mismatch between simulated and measured data, while ensuring that the force balance equation (3.27) remains true. This approach is summarized below:
Let $\mathbf{w}$ denote the *state variables* $\mathbf{u}$ and p in (3.27) which we refer to here as the *physical forward model* $\mathcal{M}(\mathbf{w})$. This forward model also depends on material parameters in (3.31) and the active contraction parameters in (3.34) or (3.37). We refer to these parameters as the *control parameters* μ and can therefore express the forward model in the form, $\mathcal{M}(\mathbf{w}, \mu) = 0$. Next we define the objective functional $\mathcal{J}(\mathbf{w}, \mu)$ as

$$\mathcal{J}(\mathbf{w}, \mu) = \alpha \mathcal{J}_{\text{volume}}(\mathbf{w}, \mu) + \beta \mathcal{J}_{\text{strain}}(\mathbf{w}, \mu) + \lambda \mathcal{J}_{\text{reg}}(\mu), \tag{3.38}$$

$$\begin{aligned} \mathcal{J}_{\text{volume}}(\mathbf{w}, \mu) &= \left(\frac{V_{\text{LV}} - \tilde{V}_{\text{LV}}}{V_{\text{LV}}} \right)^2 + \left(\frac{V_{\text{RV}} - \tilde{V}_{\text{RV}}}{V_{\text{RV}}} \right)^2, \\ \mathcal{J}_{\text{strain}}(\mathbf{w}, \mu) &= \sum_{j=1}^{3} \left(\varepsilon_j - \tilde{\varepsilon}_j \right)^2, \end{aligned} \tag{3.39}$$

where, $\mathcal{J}_{\text{volume}}(\mathbf{w}, \mu)$ is the sum of the squared relative volume error in the LV and RV, $\mathcal{J}_{\text{strain}}(\mathbf{w}, \mu)$ is the total squared strain error in the three material regions (i.e. LVFW, RVFW, and SEPT) and $\mathcal{J}_{\text{reg}}(\mu)$ is a regularization term that penalizes large variations in the control parameter for numerical stability. The accented terms in (3.39) represent the simulated values while the other terms are the measured values gotten from the patient. The weights α, β and λ control what term is favoured in the optimization. Note that the definition of the objective functional in this way is referred to as *the weighted sum method* which can be used in an optimization problem where multiple observations (or objectives) are to be minimized; in this case, the volume and strain observations.
The simulated cavity volume is given by the expression

$$\tilde{V} = -\frac{1}{3} \int_{\partial\Omega_{\text{endo}}} (\mathbf{X} + \mathbf{u}) J \mathbf{F}^{-\top} \mathbf{N} \, \mathrm{d}S, \tag{3.40}$$

while the simulated averaged normal strain in one material region Ω_j is given by the expression

$$\tilde{\varepsilon}_j = \frac{1}{|\Omega_j|} \int_{\Omega_j} \mathbf{e}_\mathrm{k}.\mathbf{E}\mathbf{e}_\mathrm{k} \, \mathrm{d}V, \tag{3.41}$$

where $\mathbf{E}$ is the Green-Lagrange strain tensor, and $\mathbf{e}_\mathrm{k}$ denotes the unit vector field in the chosen strain direction. In this thesis, the circumferential direction was chosen for the data assimilation.
Minimizing the objective functional in (3.38) while ensuring that the forward model is satisfied is referred to as a PDE-constrained optimization and can be formally stated as

$$\begin{aligned} \underset{\mu}{\text{minimize}} \quad & \mathcal{J}(\mathbf{w}, \mu) \\ \text{subject to} \quad & D\boldsymbol{\Pi}(\mathbf{u}, p) = 0. \end{aligned} \tag{3.42}$$

In this thesis we use the gradient descent method to solve this optimization problem with the following steps:

1. Solve the forward model $\mathcal{M}(\mathbf{w}, \mu) = 0$ for some initial guess μ_0 to obtain $\mathbf{w}_0$.
2. Compute the cost function $\mathcal{J}(\mathbf{w}_0, \mu_0)$.
3. Compute the gradient $D\mathcal{J}(\mathbf{w}_0, \mu_0)$ to find the direction of the steepest descent. Note that the negative of the gradient gives the direction of steepest descent.
4. Move along this direction and update the initial guess μ_0 until we reach a minimum for the cost function.

It should be noted that the minimum found using this method is not necessarily the global minimum of the function (except the function is convex with respect to the control parameters). This approach mostly converges towards a local minimum of the function which is convenient for our case.

3.4.1 Computing the Gradient of the Cost Function

Computing the functional gradient is the same as finding the derivative of the cost function with respect to the control parameters. By the chain rule we have the functional gradient $D\mathcal{J}(\mathbf{w}, \mu)$ as

$$\frac{\mathrm{d}\mathcal{J}}{\mathrm{d}\mu} = \frac{\partial \mathcal{J}}{\partial \mu} + \frac{\partial \mathcal{J}}{\partial \mathbf{w}} \frac{\mathrm{d}\mathbf{w}}{\mathrm{d}\mu}. \tag{3.43}$$

The terms $\frac{\partial \mathcal{J}}{\partial \mu}$ and $\frac{\partial \mathcal{J}}{\partial \mathbf{w}}$ are straight-forward to compute, however computing the term $\frac{\mathrm{d}\mathbf{w}}{\mathrm{d}\mu}$ requires first a solution of the force-balance equation (3.27) to determine $\mathbf{w}$. This will be computationally expensive if we have several control parameters i.e. for N control parameters we will then have to solve the force-balance equation N + 1 times. However, by using an adjoint model, we will be able to derive a linear system (linear in μ) which eliminates the need to solve the $\frac{\mathrm{d}\mathbf{w}}{\mathrm{d}\mu}$ term, thus extremely reducing the number of computations needed to compute the functional gradient. The method is explained below, for a detailed description we refer to the books by Kyung K. Choi and Nam-Ho Kim [17, 18].

The total derivative of the force balance equation with respect to the control parameter is given as

$$\frac{\mathrm{d}\mathcal{M}}{\mathrm{d}\mu} = \frac{\partial \mathcal{M}}{\partial \mathbf{w}} \frac{\mathrm{d}\mathbf{w}}{\mathrm{d}\mu} + \frac{\partial \mathcal{M}}{\partial \mu} = 0. \tag{3.44}$$

If we assume that $\frac{\partial \mathcal{M}}{\partial \mathbf{w}}$ is everywhere nonsingular, then we can re-write the expression as

$$\frac{\mathrm{d}\mathbf{w}}{\mathrm{d}\mu} = -\left(\frac{\partial \mathcal{M}}{\partial \mathbf{w}}\right)^{-1} \frac{\partial \mathcal{M}}{\partial \mu}. \tag{3.45}$$

Substituting this relationship into (3.43) yields

$$\frac{\mathrm{d}\mathcal{J}}{\mathrm{d}\mu} = \frac{\partial \mathcal{J}}{\partial \mu} - z^* \frac{\partial \mathcal{M}}{\partial \mu}, \tag{3.46}$$

where

$$z^* = -\frac{\partial \mathcal{J}}{\partial \mathbf{w}} \left(\frac{\partial \mathcal{M}}{\partial \mathbf{w}}\right)^{-1}. \tag{3.47}$$

This equation is a row vector times a square (nonsingular) matrix and using linear algebra this can be understood as the solution to the linear equation

$$\left(\frac{\partial \mathcal{M}}{\partial \mathbf{w}}\right)^* z = -\left(\frac{\partial \mathcal{J}}{\partial \mathbf{w}}\right)^*, \tag{3.48}$$

where $(.)^*$ is the Hermitian transpose also called the matrix *adjoint*, z^* is a vector of *adjoint variables* enforcing the PDE constraint and (3.48) is the *adjoint equation*. Therefore, to compute the functional gradient we first solve for z, then insert z^* in (3.46). This way, computing the gradient requires only one additional solve of a linearized system (i.e. Equation (3.48)) that is independent of the number of control parameters.

3.4.2 Parameter Estimation

We have described the mathematical model for cardiac mechanics and the methods used to assimilate patient data into the model. As part of the data assimilation process, we need to estimate the elastic material parameters (a, b, a_f, b_f) in (3.30) and the active contraction parameter [T_a in (3.34) or γ in (3.37)] for the active stress and active strain model respectively, as these parameters cannot be extracted *in vivo*. The data assimilation procedure was divided into two phases; a passive and an active phase. In the passive phase, we estimated only the linear isotropic material parameter a with an initial guess value of 1.291 kPa and the other three material parameters were fixed at $a_f = 2.582$ kPa, $b = b_f = 5.0$ kPa according to the work by Asner et al[6]. The cost function, Equation (3.38) was minimized using a as the control parameter with the weights set as $\alpha = 1.0$, $\beta = 0.0$, and $\lambda = 10^{-6}$ so that only volumes were used for the fitting. Once an optimal value was achieved for a, the material parameter was fixed and the active contraction parameter (T_a or γ) with an initial guess of zero, was set as the control parameter for the active phase of the data assimilation. The weights were set to $\alpha = 0.1$, $\beta = 1.0$, and $\lambda = 10^{-4}$ for this phase so that both volume and strain were used for the optimization. Note that the parameter estimated in the passive phase was spatially resolved on the LV (i.e LVFW + SEPT) and RVFW while the parameter in the active phase was spatially resolved on the LVFW, RVFW and septum separately.

The set of parameters (both active and passive) that yield the closest fit between model and measured volume and regional strains is taken to be the optimal set, and is used to extract biomarkers (such as ventricular wall stress).

3.5 Implementation Details

The computational modelling framework used in this thesis is called pulse-adjoint [26] and it has also been used in previous studies [11, 25]. A Galerkin finite element method with Taylor-Hood tetrahedral elements [46] (i.e. a piecewise quadratic vector field for the displacement and a piecewise linear scalar field for the pressure) was employed to find a numerical solution to the force-balance equations (3.24) and (3.25). The software implementation of the finite element method is based on the package FEniCS [66], which automatically generates matrix and vector assembly code from a symbolic representation of the force-balance equations. The resulting non-linear system of equations were solved using a Newton trust region algorithm [13] which linearizes the equations. The linear system of equations was solved by LU decomposition using a scalable distributed-

memory sparse direct solver [64].

To solve the PDE-constrained optimization problem, sequential least squares programming (SLSQP) as implemented in [59] and wrapped in the package SciPy [56] was used. dolfin-adjoint [24] was used to automatically derive the discrete adjoint system of equations from the discrete forward (force-balance) equations and compute the functional gradient needed in the SLSQP algorithm. The simulations were performed on the Abel Cluster, owned by the University of Oslo and Uninett/Sigma2, and operated by the Department for Research Computing at USIT, the University of Oslo IT-department[1]. The full source code is publicly available[2].

[1] `http://www.hpc.uio.no/`
[2] `https://github.com/ComputationalPhysiology/pulse_adjoint`

4 Results and Discussion

In this section, we present the results from the model personalization process. All simulations were performed on the Abel computing cluster using 1 node with 8 cores (with 4 GiB memory per core). The run times for the simulations are presented in Table 4.1. Note that results for the subject MR015 are not presented due to reasons discussed in Section 3.1.3.

4.1 Matching of Simulated and Measured Data

The simulated and measured pressure-volume (PV) loops of the LV and RV are shown in Figures 4.1 and 4.2 for the active stress and active strain approach respectively. We were able to achieve a very good fit using both approaches across all the subjects, with the largest error in predicted volume being 6.49 ml as shown in Table 4.2. A good fit was also achieved for the circumferential strain in the LV, RV and septum as shown graphically in Figure 4.3. Note that the time points on the horizontal axis refer to the different points at which strain was measured during a cardiac cycle. The average absolute error in the simulated circumferential strain using both approaches is shown

Patient ID	Active model	Mesh elements	Total run time, hrs
MR011	Active stress	7686	15.07
	Active strain	7686	4.95
MR016	Active stress	4126	4.22
	Active strain	4126	2.5
MR019	Active stress	4696	14.63
	Active strain	4696	4.47

Table 4.1: Timings for the simulations running on 1 computing node with 8 cores (with 4 GiB memory per core) for the different subjects and active contraction model.

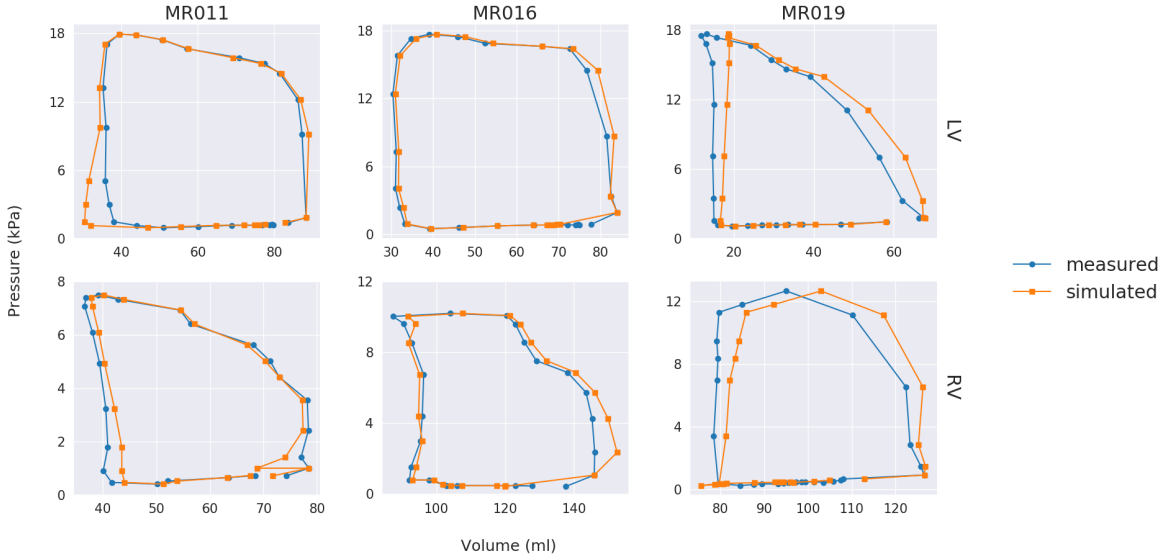

Figure 4.1: Simulated and measured pressure volume (PV) loops in the left ventricle (top row), and right ventricle (bottom row). Simulated values are based on the active stress approach.

in Table 4.2. Overall, circumferential strain matching on the LV, RV and septum was better for MR011 and MR016 compared to MR019. The maximum error in predicted values for MR011 and MR016 was 0.023 and 0.022 respectively, while for MR019 the maximum error was double that of MR011 and MR016 with a value of 0.046. One possible reason for the relatively poor fit of the circumferential strain in MR019 could be the weighted sum method used for solving the multi-objective optimization problem (discussed in Section 3.4). This method involves a trade-off when fitting both the volume and strain data in the combined objective functional and the solution found depends on the chosen weights of each objective. An exhaustive search to determine the optimum combination of weights (for the volume and strain functionals) for each subject was not performed in this thesis. Rather, the weights were fixed across all subjects and were based on values used in a previous study [26].

4.2 Validation of Computational Models

Although available, we chose not to use the longitudinal and radial strain data in the optimization. Hence, to validate the model, we compared the measured and simulated longitudinal and radial strains to determine how closely the model predicts strain. The comparison is shown graphically in Figure 4.4. Moreover, the average absolute error of

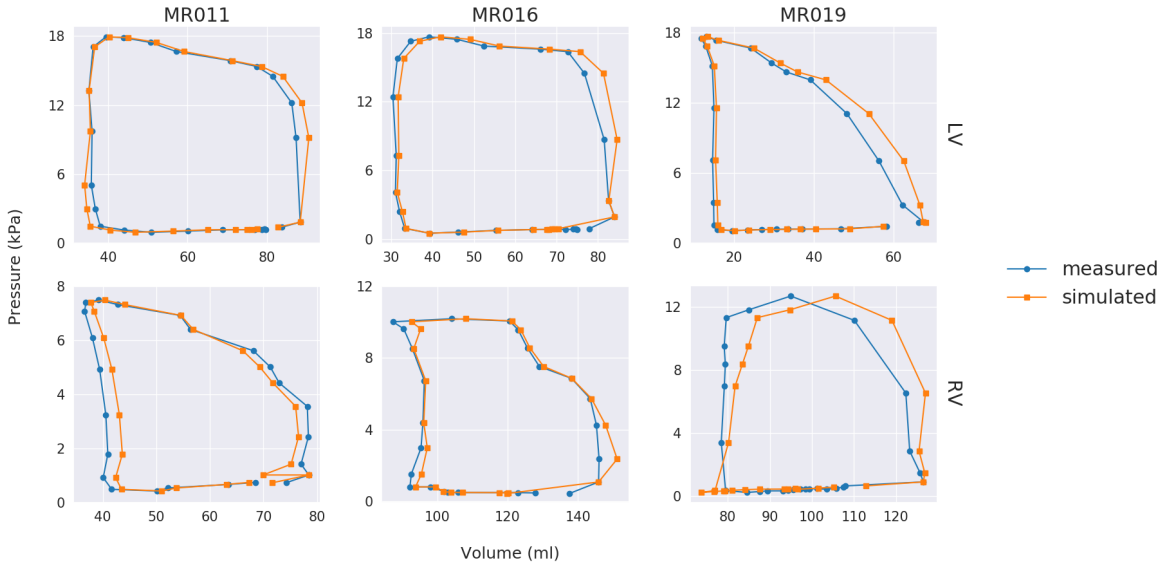

Figure 4.2: Simulated and measured pressure volume (PV) loops in the left ventricle (top row), and right ventricle (bottom row). Simulated values are based on the active strain approach.

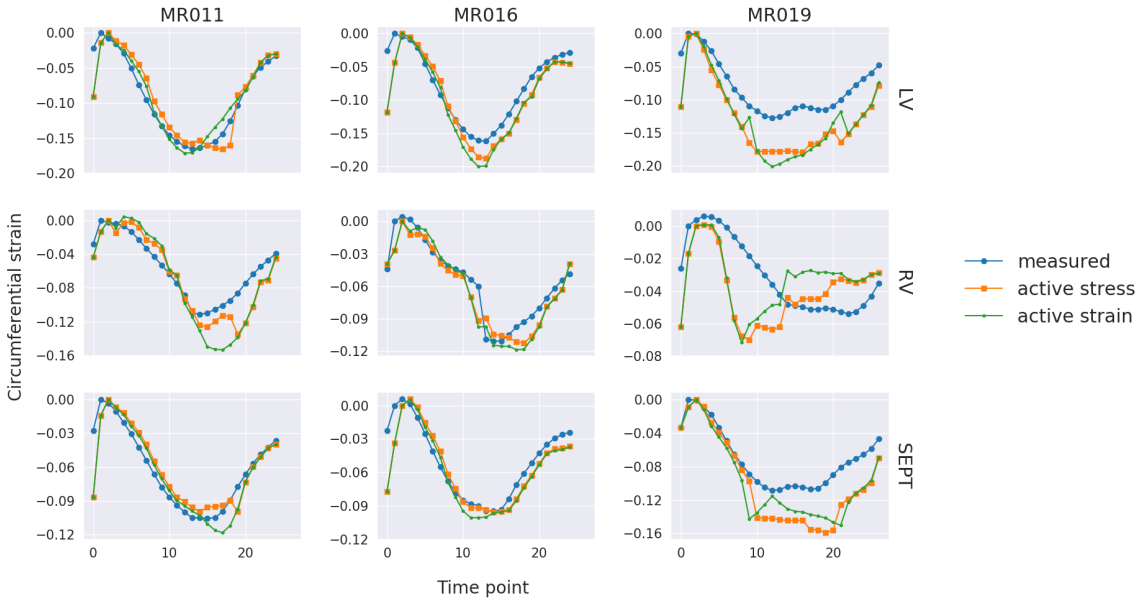

Figure 4.3: Comparison of the simulated and measured circumferential strain in the left ventricle (top row), right ventricle (middle row), and septum (bottom row). Simulated results are based on the active stress (orange lines) and active strain (green lines) approaches.

the predicted strain is given in Table 4.2. For the longitudinal strain, we see that the best fit is produced on the LV across the three subjects (using both approaches). The predicted longitudinal strain on the LV is a maximum of 0.028 off the measured strain, while for the RV and septum, it is 0.041 and 0.071 off the measured strain respectively. This is possibly due to method used in assigning fibre orientation to the biV model. The rule-based algorithm used in assigning myocardial fibre orientation to the biV model (see Section 3.1.2) is based on histological data collected from the LV. Hence, estimation of fibre angles on the RV and septum might not be as accurate as in the LV, and this may explain the less accurate predictions of strain in those regions. The radial strains were less closely predicted compared to the longitudinal strains, with the predicted strain being up to 0.466 off the measured strain. This error was recorded for MR019 and it is noted that the error in radial strain prediction was less for MR011 (maximum of 0.162) and MR016 (maximum of 0.143) compared to MR019.

Overall, longitudinal and radial strain prediction was less accurate for MR019 compared to MR011 and MR016. This could possibly be due to the relatively poor data matching (of volume and circumferential strain discussed in Section 4.1) for that subject. Further, the active stress approach generally predicted longitudinal and radial strain better than the active strain approach across the three subjects, based on the quantified errors shown in Table 4.2.

4.3 Active Stress vs. Active Strain Models

Time traces of the average *Cauchy* fiber stress on the LV and RV using both approaches are shown in Figure 4.5 for the three subjects. Overall, the active stress formulation predicts higher peak stresses compared to the active strain formulation (except for results on the LV of MR019). The difference in peak stress prediction is more pronounced in the LV, as was also observed in a previous study [26]. In Figure 4.6 and Figure 4.7, we compare the average circumferential stress and average longitudinal stress respectively, using the two formulations. Both approaches predicted similar stresses in the circumferential and longitudinal directions (with only slight variations), except for the predicted results on the LV of MR019. However, there was no similar correlation in the radial stress prediction, with the active strain formulation estimating higher radial stresses as shown in Figure 4.8. Note that the inconsistency observed in the stress predictions on MR019 could possibly be a consequence of the relatively poor data-fitting for that subject.

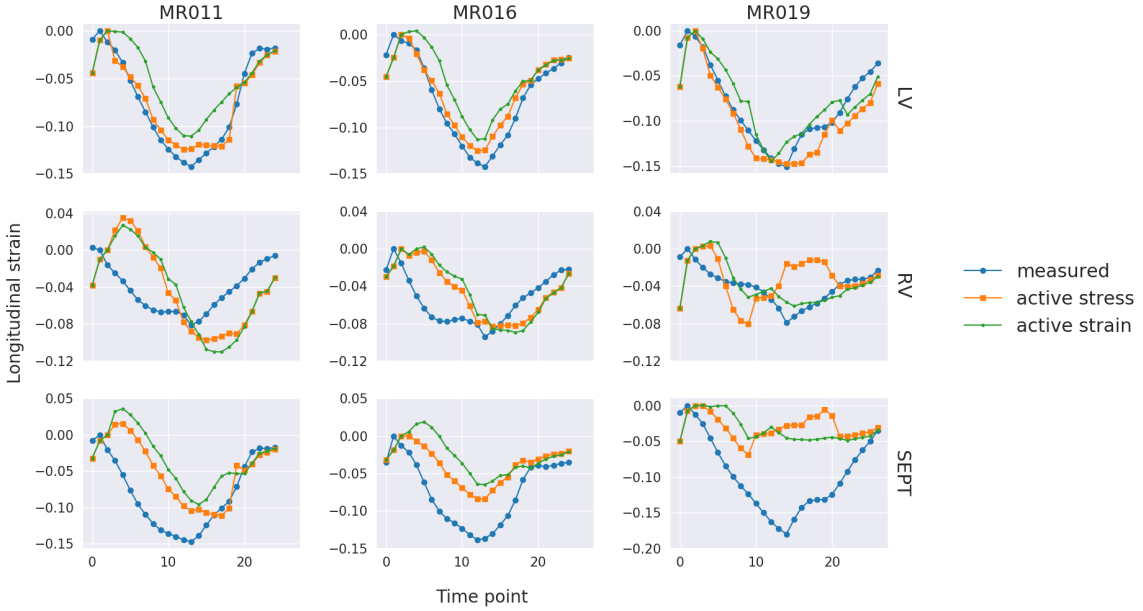

(a)

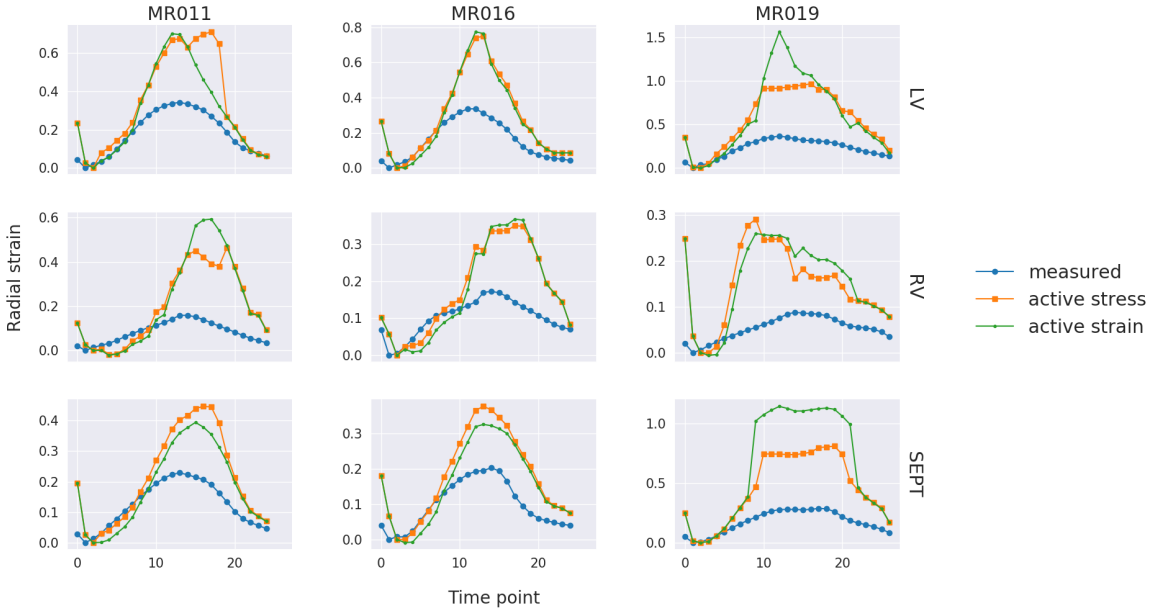

(b)

Figure 4.4: Validation of the model personalization process using simulated and measured **(a)** longitudinal strain and **(b)** radial strain in the left ventricle (top row), right ventricle (middle row), and septum (bottom row). The measured longitudinal and radial strains were not used in the optimization and the simulated results are based on the active stress (orange lines) and active strain (green lines) approaches.

Patient ID	Active model	Region	Avg. absolute volume error (mL)	Avg. absolute strain error		
				Circumferential strain	Longitudinal strain	Radial strain
MR011	Active stress	LV	2.66	0.015	0.012	0.161
		RV	1.63	0.016	0.038	0.138
		SEPT	-	0.010	0.037	0.096
	Active strain	LV	2.10	0.011	0.028	0.115
		RV	1.83	0.023	0.041	0.162
		SEPT	-	0.010	0.052	0.079
MR016	Active stress	LV	1.89	0.020	0.012	0.140
		RV	3.05	0.011	0.024	0.085
		SEPT	-	0.010	0.036	0.085
	Active strain	LV	2.44	0.022	0.024	0.143
		RV	2.73	0.011	0.029	0.090
		SEPT	-	0.011	0.048	0.074
MR019	Active stress	LV	2.92	0.046	0.016	0.345
		RV	5.54	0.020	0.024	0.099
		SEPT	-	0.029	0.071	0.284
	Active strain	LV	1.80	0.045	0.017	0.390
		RV	6.49	0.022	0.013	0.106
		SEPT	-	0.027	0.068	0.466

Table 4.2: Error quantification for the simulated volume as well as the simulated circumferential, longitudinal and radial strains. The average absolute error is computed as $\frac{\sum_{i=1}^{n}|s_i - m_i|}{n}$, where s_i and m_i are the simulated and measured values respectively and n is the number of sample points.

Significant differences were observed in how both formulations predicted deviatoric stress as shown in Figure 4.9 for MR016. Similar differences were observed for the other two subjects (MR011 and MR019) used in this study. Note that the deviatoric component of the total *Cauchy* stress (σ) is made up of all the terms in Equation 3.31 except the *Lagrange multiplier* term ($p\mathbf{I}$). To determine if the nodes at the model extremities (i.e. the basal boundary and apex) played a role in creating these significant differences, we took a slice approximately midway through the biV model (see Figure 4.10a) and extracted the deviatoric stress in the fibre, circumferential, longitudinal and radial directions. As shown in Figure 4.10b, deviatoric stress prediction still varied significantly along the slice between the active stress and active strain formulations. This suggests that the model extremities and boundary conditions do not affect the extracted stress results. Since the total *Cauchy* stress prediction is fairly close between the active stress and active strain formulations, a possible explanation for the difference

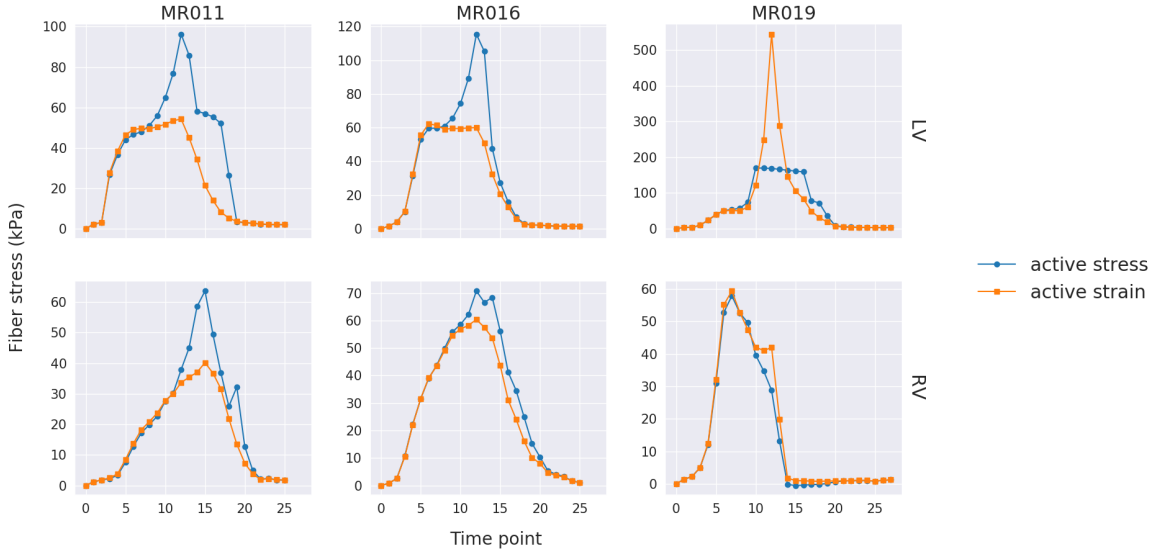

Figure 4.5: Estimated *Cauchy* fiber stress in the left ventricle (top row) and right ventricle (bottom row) using the active stress (blue lines) and active strain (orange lines) formulation.

in deviatoric stress prediction between the two formulations can be as a result of the incompressibility constraint imposed on the model. In the active stress formulation, the resultant hydrostatic pressure (p) applied to ensure constant volume is much higher than that required for the active strain formulation as shown in Figure 4.11. This directly impacts the value of the deviatoric stress component in (3.31,) as a larger p ultimately implies a higher deviatoric stress prediction.

4.3.1 Active Stress vs. Active Strain for a Simple Case of a Contracting Tissue Cube

To show that both formulations can produce similar stress predictions in a simplified setting, we considered the case of a tissue cube with uniform fibre orientation aligned with one of the principal axes. The cube was assumed to be fully incompressible, with a uniform deformation state. It was assumed to contract against a linear spring force while being unloaded in the transverse directions. A detailed derivation of the *Cauchy* stress tensor and force balance equation based on the active stress and active strain formulations for this simplified case is provided in Appendix A.

By tuning the active stress and active strain parameters in Equations 3.34 and 3.37 respectively, we matched the deformation of the tissue cube using both approaches as

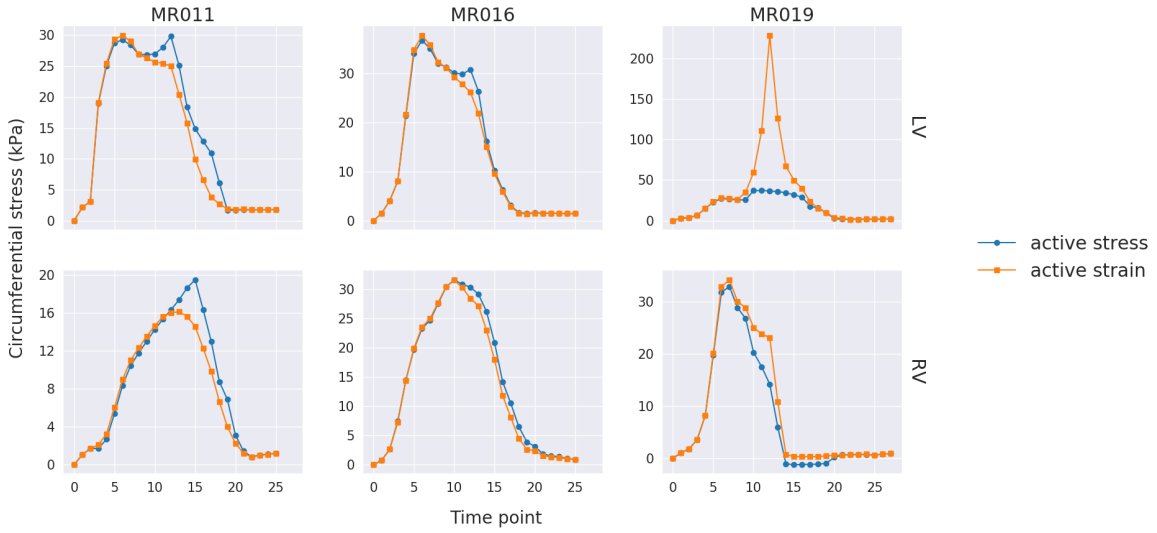

Figure 4.6: Estimated circumferential stress in the left ventricle (top row) and right ventricle (bottom row) using the active stress (blue lines) and active strain (orange lines) formulation.

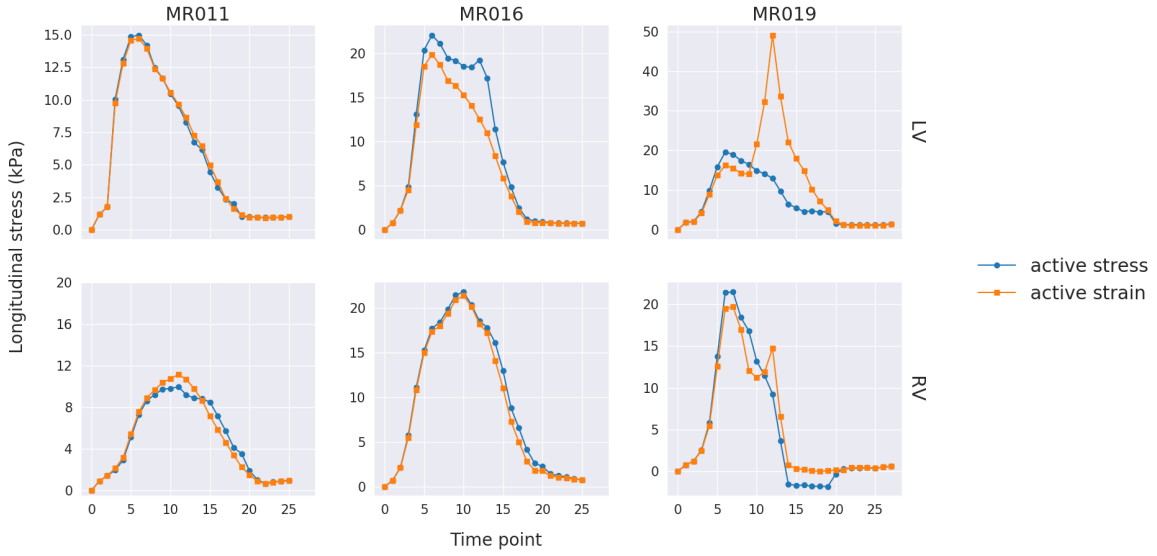

Figure 4.7: Estimated longitudinal stress in the left ventricle (top row) and right ventricle (bottom row) using the active stress (blue lines) and active strain (orange lines) formulation.

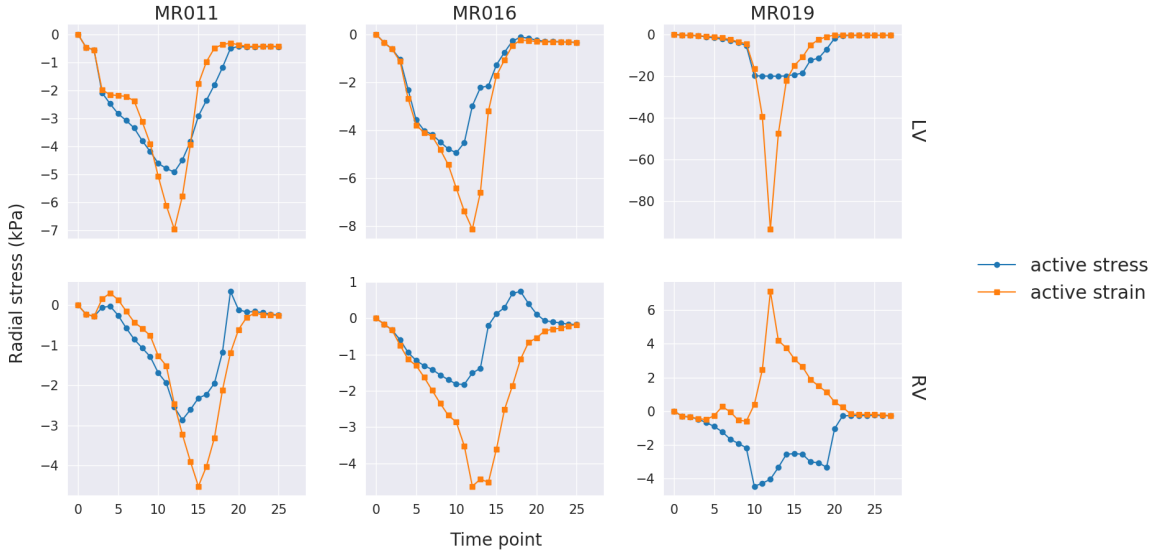

Figure 4.8: Estimated radial stress in the left ventricle (top row) and right ventricle (bottom row) using the active stress (blue lines) and active strain (orange lines) formulation.

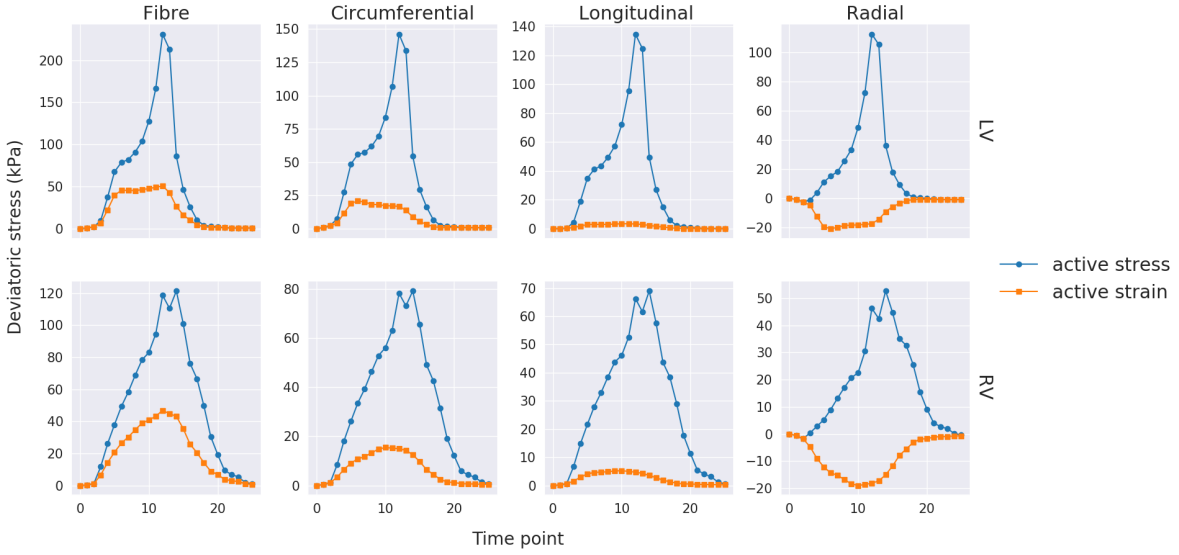

Figure 4.9: Estimated deviatoric stress in the left ventricle (top row) and right ventricle (bottom row) of MR016 using the active stress (blue lines) and active strain (orange lines) formulation. The columns represent the stress in the fibre, circumferential, longitudinal and radial directions.

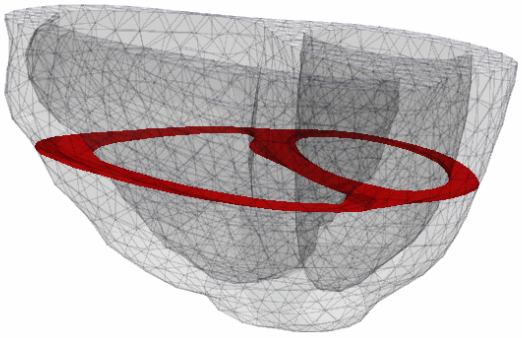

(a)

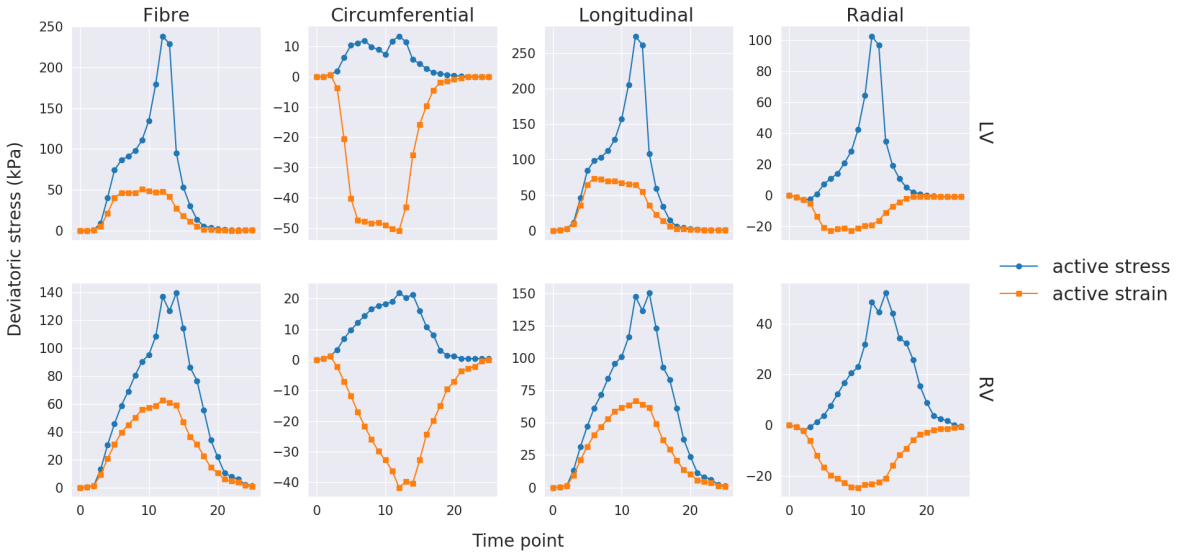

(b)

Figure 4.10: (a) A slice (in red) approximately midway through the biV model used to extract deviatoric stress results away from the model extremities. **(b)** Estimated deviatoric stress in the left ventricle (top row) and right ventricle (bottom row) on the slice shown in (a) using the active stress (blue lines) and active strain (orange lines) formulation. The columns represent the stress in the fibre, circumferential, longitudinal and radial directions.

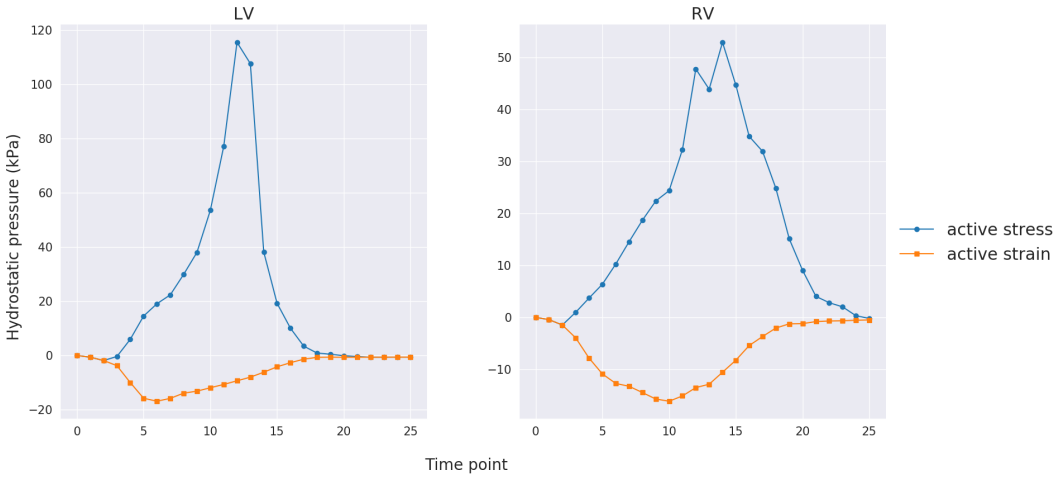

Figure 4.11: Hydrostatic pressure on the LV and RV using the active stress (blue lines) and active strain (orange lines) formulations.

shown in the left panel of Figure 4.12. Consequently, this produced similar *Cauchy* stress prediction using both approaches as shown in the right panel of Figure 4.12. Such manual parameter tuning might not be feasible in a personalized heart model due to the complex geometry and myofibre orientation. However, the sole aim of this experiment was to show that despite the fundamentally different formulations for the active stress and active strain approaches to modelling active contraction, they can produce similar stress predictions in a simplified case.

4.4 Limitations and Future Directions

We have used a fully incompressible model of the myocardium, although it is well known that the myocardium is compressible due to perfusion of blood [115]. We observe large differences in the hydrostatic stress component between the two approaches, and it is possible that the differences in the total stress are largely caused by the incompressibility constraint. Future studies could therefore investigate the role of compressibility on stress predictions of the two approaches, and compare the *Lagrange multiplier* method applied here to alternative approaches such as the *penalty method* for quasi-incompressibility [90]).

In assigning myocardial fibre orientation to the biV model, we used a rule-based algorithm which was based on histological data for only the LV. For this reason, the

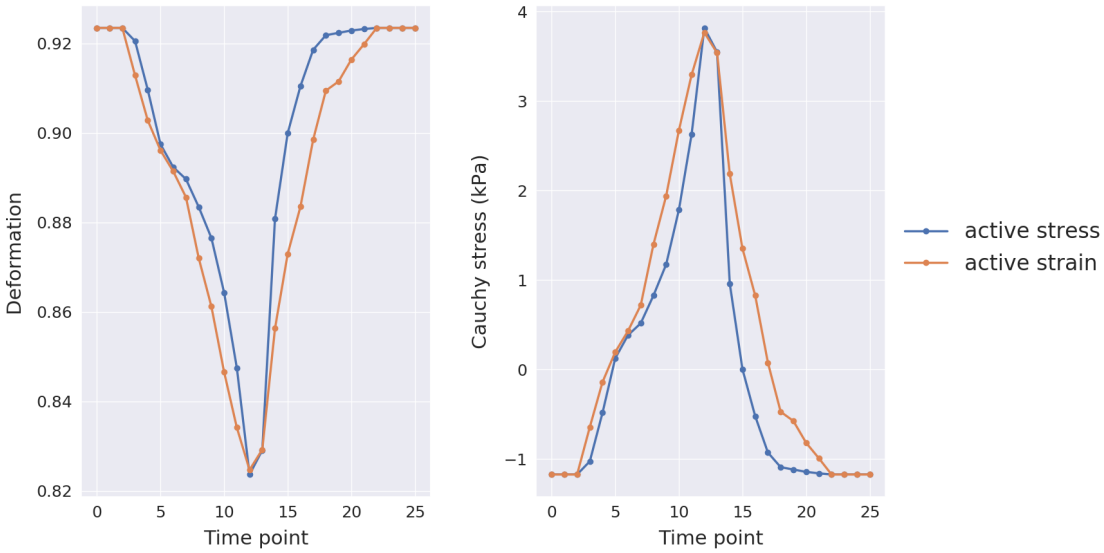

Figure 4.12: Left: Deformation of tissue cube under spring load using the active stress and active strain formulations. Right: *Cauchy* stress on the tissue cube as a result of the deformations using the active stress (blue lines) and active strain (orange lines) formulation.

estimated fibre angles on the RV and septum may not be as close to actual values. A sensitivity analysis to determine the effect of this on the model predictions would be beneficial and should be carried out in future studies. Equally, a rule-based algorithm that estimates fibre angles on the LV, RV and septum independently could be implemented in future studies, or if possible, *in vivo* measures of fibre angles could be used.

As noted, the weights used in the multi-objective functional (3.38) were based on a previous study [26] and may not have been the optimal choice for the dataset used in this thesis. We achieved a good data-matching for two subjects (MR011 and MR016), while a relatively poor fit was observed for MR019. The poorly fitted strains may have led to inconsistencies in the predicted results. Future studies could conduct sensitivity analysis by testing different weight combinations for the strain and volume functionals to obtain an optimum combination. Also, other general methods for solving multi-objective optimization problems (see [67]) may provide superior results to those of the weighted sum method and could be considered in future studies.

Further, only the model predicted ventricular wall stress was compared between the two formulations in this thesis. It would be beneficial to investigate if differences exist in the prediction of other mechanical features such as ventricular elastance or regional myocardial work using both formulations. This could be explored in future studies.

5 Conclusion

We have used a computational modelling and data assimilation framework, to produce a similar set of patient-specific models of cardiac mechanics, but using the active stress and active strain approaches to modelling cardiac contraction. We used these personalized models to compared stress prediction using both approaches, and found that fibre, circumferential and longitudinal total stress predictions (Figures 4.5 to 4.7) were closely matched between the two approaches for the subjects used this thesis. Peak fibre stress in Figure 4.5, was however, higher using the active stress approach, which proved to be consistent with the literature [26]. On the other hand, predictions of total radial stress in Figure 4.8, and the deviatoric component of the total stress in the fibre, circumferential, longitudinal and radial directions (Figure 4.9), were significantly different between both approaches for all the subjects. It is noted that inconsistencies were observed in the results produced for one of the subjects (MR019), especially on the LV. This could possibly be attributed to the relatively poor data matching (for that subject) during the data assimilation, or noise in the clinical data.

Moreover, we were able to show in Section 4.3.1 that in a simplified setting, such as the contraction of a tissue cube, both approaches can produce similar stress predictions (Figure 4.12) by tuning the active stress and active strain parameters in order to match the deformation produced, and by extension, the stress prediction using both approaches.

Due to the limitations discussed in Section 4.4, we cannot conclude that one approach is better than the other in modelling cardiac contraction. The active stress approach produced a better strain prediction as shown in Table 4.2, however, as we do not have measured stress values for the subjects, it is not possible to say which approach predicted stress better. On the other hand, we can conclude that differences exist in the stress prediction using both approaches. Future work could be used to compare how closely both approaches predict other mechanical features such as ventricular elastance and regional myocardial work. Also, the effect of compressibility on stress prediction using the two approaches could be explored in a future study.

Bibliography

[1] inHeart: In Silico Heart Failure - Tools for Accelerating Biomedical Research — Simula. https://www.simula.no/research/projects/inheart-silico-heart-failure-tools-accelerating-biomedical-research.

[2] MI-RISK: Risk factors for sudden cardiac death during acute myocardial infarction — Simula. https://www.simula.no/research/projects/mi-risk-risk-factors-sudden-cardiac-death-during-acute-myocardial-infarction.

[3] J. Aguado-Sierra, A. Krishnamurthy, C. Villongco, J. Chuang, E. Howard, M. J. Gonzales, J. Omens, D. E. Krummen, S. Narayan, R. C. P. Kerckhoffs, and A. D. McCulloch. Patient-specific modeling of dyssynchronous heart failure: A case study. *Progress in Biophysics and Molecular Biology*, 107(1):147–155, Oct. 2011.

[4] S. S. Antman. *Nonlinear Problems of Elasticity*. Applied Mathematical Sciences. Springer-Verlag, New York, 1995.

[5] T. Arts, R. S. Reneman, and P. C. Veenstra. A model of the mechanics of the left ventricle. *Annals of Biomedical Engineering*, 7(3):299–318, May 1979.

[6] L. Asner, M. Hadjicharalambous, R. Chabiniok, D. Peresutti, E. Sammut, J. Wong, G. Carr-White, P. Chowienczyk, J. Lee, A. King, N. Smith, R. Razavi, and D. Nordsletten. Estimation of passive and active properties in the human heart using 3D tagged MRI. *Biomechanics and Modeling in Mechanobiology*, 15(5):1121–1139, Oct. 2016.

[7] K. F. Augenstein, B. R. Cowan, I. J. LeGrice, P. M. F. Nielsen, and A. A. Young. Method and Apparatus for Soft Tissue Material Parameter Estimation Using Tissue Tagged Magnetic Resonance Imaging. *Journal of Biomechanical Engineering*, 127(1):148–157, Feb. 2005.

[8] D. B. Badesch, H. C. Champion, M. A. G. Sanchez, M. M. Hoeper, J. E. Loyd, A. Manes, M. McGoon, R. Naeije, H. Olschewski, R. J. Oudiz, and A. Torbicki. Diagnosis and Assessment of Pulmonary Arterial Hypertension. *Journal of the American College of Cardiology*, 54(1 Supplement):S55–S66, June 2009.

[9] B. Baillargeon, N. Rebelo, D. D. Fox, R. L. Taylor, and E. Kuhl. The Living Heart Project: A robust and integrative simulator for human heart function. *European Journal of Mechanics - A/Solids*, 48:38–47, Nov. 2014.

[10] G. Balaban, M. S. Alnæs, J. Sundnes, and M. E. Rognes. Adjoint multi-start-based

estimation of cardiac hyperelastic material parameters using shear data. *Biomechanics and Modeling in Mechanobiology*, 15(6):1509–1521, Dec. 2016.

[11] G. Balaban, H. Finsberg, S. Funke, T. F. Håland, E. Hopp, J. Sundnes, S. Wall, and M. E. Rognes. In vivo estimation of elastic heterogeneity in an infarcted human heart. *Biomechanics and Modeling in Mechanobiology*, 17(5):1317–1329, Oct. 2018.

[12] G. Balaban, H. Finsberg, H. Henrik Odland, M. E. Rognes, S. Ross, J. Sundnes, and S. Wall. High-resolution data assimilation of cardiac mechanics applied to a dyssynchronous ventricle. *International Journal for Numerical Methods in Biomedical Engineering*, 33(11):e2863, 2017.

[13] S. Balay, S. Abhyankar, M. Adams, J. Brown, P. Brune, K. Buschelman, L. Dalcin, A. Dener, V. Eijkhout, and W. Gropp. PETSc Web page. http://www.mcs.anl.gov/petsc, 2019.

[14] J. D. Bayer, R. C. Blake, G. Plank, and N. A. Trayanova. A Novel Rule-Based Algorithm for Assigning Myocardial Fiber Orientation to Computational Heart Models. *Annals of Biomedical Engineering*, 40(10):2243–2254, Oct. 2012.

[15] E. Berberoğlu, H. O. Solmaz, and S. Göktepe. Computational modeling of coupled cardiac electromechanics incorporating cardiac dysfunctions. *European Journal of Mechanics - A/Solids*, 48:60–73, Nov. 2014.

[16] J. Bols, J. Degroote, B. Trachet, B. Verhegghe, P. Segers, and J. Vierendeels. A computational method to assess the in vivo stresses and unloaded configuration of patient-specific blood vessels. *Journal of Computational and Applied Mathematics*, 246:10–17, July 2013.

[17] K. K. Choi and N.-H. Kim. *Structural Sensitivity Analysis and Optimization 1: Linear Systems*. Mechanical Engineering Series, Structural Analysis. Springer-Verlag, New York, 2005.

[18] K. K. Choi and N.-H. Kim. *Structural Sensitivity Analysis and Optimization 2: Nonlinear Systems and Applications*. Mechanical Engineering Series, Structural Analysis. Springer-Verlag, New York, 2005.

[19] A. B. C. Dang, J. M. Guccione, P. Zhang, A. W. Wallace, R. C. Gorman, J. H. Gorman, and M. B. Ratcliffe. Effect of Ventricular Size and Patch Stiffness in Surgical Anterior Ventricular Restoration: A Finite Element Model Study. *The Annals of Thoracic Surgery*, 79(1):185–193, Jan. 2005.

[20] H. Demiray. Stresses in Ventricular Wall. *Journal of Applied Mechanics*, 43(2):194–197, June 1976.

[21] S. Dokos, B. H. Smaill, A. A. Young, and I. J. LeGrice. Shear properties of passive ventricular myocardium. *American Journal of Physiology-Heart and Circulatory Physiology*, 283(6):H2650–H2659, Dec. 2002.

[22] R. Doste, D. Soto-Iglesias, G. Bernardino, A. Alcaine, R. Sebastian, S. Giffard-Roisin,

M. Sermesant, A. Berruezo, D. Sanchez-Quintana, and O. Camara. A rule-based method to model myocardial fiber orientation in cardiac biventricular geometries with outflow tracts. *International Journal for Numerical Methods in Biomedical Engineering*, 35(4):e3185, 2019.

[23] H. W. Farber and J. Loscalzo. Pulmonary Arterial Hypertension. *New England Journal of Medicine*, 351(16):1655–1665, Oct. 2004.

[24] P. Farrell, D. Ham, S. Funke, and M. Rognes. Automated Derivation of the Adjoint of High-Level Transient Finite Element Programs. *SIAM Journal on Scientific Computing*, 35(4):C369–C393, Jan. 2013.

[25] H. Finsberg, G. Balaban, S. Ross, T. F. Håland, H. H. Odland, J. Sundnes, and S. Wall. Estimating cardiac contraction through high resolution data assimilation of a personalized mechanical model. *Journal of Computational Science*, 24:85–90, Jan. 2018.

[26] H. Finsberg, C. Xi, J. L. Tan, L. Zhong, M. Genet, J. Sundnes, L. C. Lee, and S. T. Wall. Efficient estimation of personalized biventricular mechanical function employing gradient-based optimization. *International Journal for Numerical Methods in Biomedical Engineering*, 34(7):e2982, 2018.

[27] M. H. Friedman and L. W. Ehrlich. Numerical simulation of aortic bifurcation flows: The effect of flow divider curvature. *Journal of Biomechanics*, 17(12):881–888, Jan. 1984.

[28] T. Fritz, C. Wieners, G. Seemann, H. Steen, and O. Dössel. Simulation of the contraction of the ventricles in a human heart model including atria and pericardium. *Biomechanics and Modeling in Mechanobiology*, 13(3):627–641, June 2014.

[29] N. Galiè, Task Force members, A. Torbicki, Task Force members, R. Barst, Task Force members, P. Dartevelle, Task Force members, S. Haworth, Task Force members, T. Higenbottam, Task Force members, H. Olschewski, Task Force members, A. Peacock, Task Force members, G. Pietra, Task Force members, L. J. Rubin, Task Force members, G. Simonneau, and Task Force members. Guidelines on diagnosis and treatment of pulmonary arterial hypertension: The Task Force on Diagnosis and Treatment of Pulmonary Arterial Hypertension of the European Society of Cardiology. *European Heart Journal*, 25(24):2243–2278, Dec. 2004.

[30] M. W. Gee, C. Förster, and W. A. Wall. A computational strategy for prestressing patient-specific biomechanical problems under finite deformation. *International Journal for Numerical Methods in Biomedical Engineering*, 26(1):52–72, 2010.

[31] T. Geijtenbeek, M. van de Panne, and A. F. van der Stappen. Flexible Muscle-based Locomotion for Bipedal Creatures. *ACM Trans. Graph.*, 32(6):206:1–206:11, Nov. 2013.

[32] M. Genet, L. C. Lee, R. Nguyen, H. Haraldsson, G. Acevedo-Bolton, Z. Zhang, L. Ge, K. Ordovas, S. Kozerke, and J. M. Guccione. Distribution of normal human left ventricular myofiber stress at end diastole and end systole: A target for in silico design of heart

failure treatments. *Journal of Applied Physiology*, 117(2):142–152, May 2014.

[33] C. Geuzaine and J.-F. Remacle. Gmsh: A 3-D finite element mesh generator with built-in pre- and post-processing facilities. *International Journal for Numerical Methods in Engineering*, 79(11):1309–1331, Sept. 2009.

[34] F. J. H. Gijsen, J. J. Wentzel, A. Thury, B. Lamers, J. C. H. Schuurbiers, P. W. Serruys, and A. F. van der Steen. A new imaging technique to study 3-D plaque and shear stress distribution in human coronary artery bifurcations in vivo. *Journal of Biomechanics*, 40(11):2349–2357, Jan. 2007.

[35] S. Göktepe, A. Menzel, and E. Kuhl. The Generalized Hill Model: A Kinematic Approach Towards Active Muscle Contraction. *Journal of the Mechanics and Physics of Solids*, 72:20–39, Dec. 2014.

[36] P. Gould, D. Ghista, L. Brombolich, and I. Mirsky. In vivo stresses in the human left ventricular wall: Analysis accounting for the irregular 3-dimensional geometry and comparison with idealised geometry analyses. *Journal of Biomechanics*, 5(5):521–539, Sept. 1972.

[37] S. Govindjee and P. A. Mihalic. Computational methods for inverse finite elastostatics. *Computer Methods in Applied Mechanics and Engineering*, 136(1):47–57, Sept. 1996.

[38] R. A. Gray and P. Pathmanathan. Patient-Specific Cardiovascular Computational Modeling: Diversity of Personalization and Challenges. *Journal of Cardiovascular Translational Research*, 11(2):80–88, Apr. 2018.

[39] J. M. Guccione, A. D. McCulloch, and L. K. Waldman. Passive Material Properties of Intact Ventricular Myocardium Determined From a Cylindrical Model. *Journal of Biomechanical Engineering*, 113(1):42–55, Feb. 1991.

[40] J. M. Guccione, L. K. Waldman, and A. D. McCulloch. Mechanics of Active Contraction in Cardiac Muscle: Part II—Cylindrical Models of the Systolic Left Ventricle. *Journal of Biomechanical Engineering*, 115(1):82–90, Feb. 1993.

[41] W. T. Hanna. A Simulation of Human Heart Function. *Biophysical Journal*, 13(7):603–621, July 1973.

[42] N. Hansen. The CMA Evolution Strategy: A Comparing Review. In J. A. Lozano, P. Larrañaga, I. Inza, and E. Bengoetxea, editors, *Towards a New Evolutionary Computation: Advances in the Estimation of Distribution Algorithms*, Studies in Fuzziness and Soft Computing, pages 75–102. Springer Berlin Heidelberg, Berlin, Heidelberg, 2006.

[43] Hill Archibald Vivian. The heat of shortening and the dynamic constants of muscle. *Proceedings of the Royal Society of London. Series B - Biological Sciences*, 126(843):136–195, Oct. 1938.

[44] G. A. Holzapfel. *Nonlinear Solid Mechanics: A Continuum Approach for Engineering*. Wiley, Apr. 2000.

[45] Holzapfel Gerhard A. and Ogden Ray W. Constitutive modelling of passive myocardium: A structurally based framework for material characterization. *Philosophical Transactions of the Royal Society A: Mathematical, Physical and Engineering Sciences*, 367(1902):3445–3475, Sept. 2009.

[46] P. Hood and C. Taylor. Navier-Stokes equations using mixed interpolation. *Finite element methods in flow problems*, pages 121–132, 1974.

[47] Hood William P., Thomson Walter J., Rackley Charles E., and Rolett Ellis L. Comparison of Calculations of Left Ventricular Wall Stress in Man from Thin-Walled and Thick-Walled Ellipsoidal Models. *Circulation Research*, 24(4):575–582, Apr. 1969.

[48] P. R. Hoskins. Introduction to Cardiovascular Biomechanics. In P. R. Hoskins, P. V. Lawford, and B. J. Doyle, editors, *Cardiovascular Biomechanics*, pages 25–35. Springer International Publishing, Cham, 2017.

[49] P. R. Hoskins, N. Conlisk, A. J. Geers, and B. J. Doyle. Patient Specific Modelling. In P. R. Hoskins, P. V. Lawford, and B. J. Doyle, editors, *Cardiovascular Biomechanics*, pages 207–230. Springer International Publishing, Cham, 2017.

[50] P. R. Hoskins, S. F. Keevil, and S. Mirsadraee. Medical Imaging. In P. R. Hoskins, P. V. Lawford, and B. J. Doyle, editors, *Cardiovascular Biomechanics*, pages 163–191. Springer International Publishing, Cham, 2017.

[51] P. R. Hoskins, P. V. Lawford, and B. J. Doyle, editors. *Cardiovascular Biomechanics*. Springer International Publishing, 2017.

[52] M. Humbert, O. Sitbon, and G. Simonneau. Treatment of Pulmonary Arterial Hypertension. *New England Journal of Medicine*, 351(14):1425–1436, Sept. 2004.

[53] J. D. Humphrey, R. K. Strumpf, and F. C. P. Yin. Determination of a Constitutive Relation for Passive Myocardium: I. A New Functional Form. *Journal of Biomechanical Engineering*, 112(3):333–339, Aug. 1990.

[54] J. D. Humphrey and F. C. P. Yin. On Constitutive Relations and Finite Deformations of Passive Cardiac Tissue: I. A Pseudostrain-Energy Function. *Journal of Biomechanical Engineering*, 109(4):298–304, Nov. 1987.

[55] R. F. Janz and A. F. Grimm. Finite-element model for the mechanical behavior of the left ventricle. Prediction of deformation in the potassium-arrested rat heart. *Circulation Research*, 30(2):244–252, Feb. 1972.

[56] E. Jones, T. Oliphant, and P. Peterson et al. SciPy: Open source scientific tools for Python. "http://www.scipy.org/", (2001–).

[57] A. M. Katz. *Physiology of the Heart*. Lippincott Williams & Wilkins, Nov. 2010.

[58] Kohl P., Noble D., Hunter P. J., Costa K. D., Holmes J. W., and Mcculloch A. D. Modelling cardiac mechanical properties in three dimensions. *Philosophical Transactions of the Royal Society of London. Series A: Mathematical, Physical and Engineering Sciences*,

359(1783):1233–1250, June 2001.

[59] D. Kraft. A software package for sequential quadratic programming. *Forschungsbericht-Deutsche Forschungs- und Versuchsanstalt fur Luft- und Raumfahrt*, 1988.

[60] Krams R., Wentzel J.J., Oomen J.A.F., Vinke R., Schuurbiers J.C.H., de Feyter P.J., Serruys P.W., and Slager C.J. Evaluation of Endothelial Shear Stress and 3D Geometry as Factors Determining the Development of Atherosclerosis and Remodeling in Human Coronary Arteries in Vivo. *Arteriosclerosis, Thrombosis, and Vascular Biology*, 17(10):2061–2065, Oct. 1997.

[61] S. Land et al. Verification of cardiac mechanics software: Benchmark problems and solutions for testing active and passive material behaviour. *Proceedings of the Royal Society A: Mathematical, Physical and Engineering Sciences*, 471(2184):20150641, Dec. 2015.

[62] P. Le Tallec. Existence and approximation results for nonlinear mixed problems: Application to incompressible finite elasticity. *Numerische Mathematik*, 38(3):365–382, Oct. 1982.

[63] L. C. Lee, L. Ge, Z. Zhang, M. Pease, S. D. Nikolic, R. Mishra, M. B. Ratcliffe, and J. M. Guccione. Patient-specific finite element modeling of the Cardiokinetix Parachute® device: Effects on left ventricular wall stress and function. *Medical & Biological Engineering & Computing*, 52(6):557–566, June 2014.

[64] X. S. Li and J. W. Demmel. SuperLU_DIST: A Scalable Distributed-memory Sparse Direct Solver for Unsymmetric Linear Systems. *ACM Trans. Math. Softw.*, 29(2):110–140, June 2003.

[65] D. H. S. Lin and F. C. P. Yin. A Multiaxial Constitutive Law for Mammalian Left Ventricular Myocardium in Steady-State Barium Contracture or Tetanus. *Journal of Biomechanical Engineering*, 120(4):504–517, Aug. 1998.

[66] A. Logg, K.-A. Mardal, and G. Wells. *Automated Solution of Differential Equations by the Finite Element Method: The FEniCS Book*. Springer Science & Business Media, Feb. 2012.

[67] R. Marler and J. Arora. Survey of multi-objective optimization methods for engineering. *Structural and Multidisciplinary Optimization*, 26(6):369–395, Apr. 2004.

[68] I. Mirsky. Left Ventricular Stresses in the Intact Human Heart. *Biophysical Journal*, 9(2):189–208, Feb. 1969.

[69] I. Mirsky. Ventricular and Arterial Wall Stresses Based on Large Deformation Analyses. *Biophysical Journal*, 13(11):1141–1159, Nov. 1973.

[70] D. Mojsejenko, J. R. McGarvey, S. M. Dorsey, J. H. Gorman, J. A. Burdick, J. J. Pilla, R. C. Gorman, and J. F. Wenk. Estimating passive mechanical properties in a myocardial infarction using MRI and finite element simulations. *Biomechanics and*

Modeling in Mechanobiology, 14(3):633–647, June 2015.

[71] R. Molléro, X. Pennec, H. Delingette, A. Garny, N. Ayache, and M. Sermesant. Multifidelity-CMA: A multifidelity approach for efficient personalisation of 3D cardiac electromechanical models. *Biomechanics and Modeling in Mechanobiology*, 17(1):285–300, Feb. 2018.

[72] S. E. Moskowitz. Effects of inertia and viscoelasticity in late rapid filling of the left ventricle. *Journal of Biomechanics*, 14(6):443–445, Jan. 1981.

[73] A. U. Nair, D. G. Taggart, and F. J. Vetter. Optimizing cardiac material parameters with a genetic algorithm. *Journal of Biomechanics*, 40(7):1646–1650, Jan. 2007.

[74] P. Nardinocchi and L. Teresi. On the Active Response of Soft Living Tissues. *Journal of Elasticity*, 88(1):27–39, July 2007.

[75] M. L. Neal and R. Kerckhoffs. Current progress in patient-specific modeling. *Briefings in Bioinformatics*, 11(1):111–126, Jan. 2010.

[76] S. Nielles-Vallespin, C. Mekkaoui, P. Gatehouse, T. G. Reese, J. Keegan, P. F. Ferreira, S. Collins, P. Speier, T. Feiweier, R. de Silva, M. P. Jackowski, D. J. Pennell, D. E. Sosnovik, and D. Firmin. In vivo diffusion tensor MRI of the human heart: Reproducibility of breath-hold and navigator-based approaches. *Magnetic Resonance in Medicine*, 70(2):454–465, 2013.

[77] P. M. Nielsen, I. J. Le Grice, B. H. Smaill, and P. J. Hunter. Mathematical model of geometry and fibrous structure of the heart. *American Journal of Physiology-Heart and Circulatory Physiology*, 260(4):H1365–H1378, Apr. 1991.

[78] M. Okajima, T. Fujino, T. Kobayashi, and K. M. T. Yamada. Computer simulation of the propagation process in excitation of the ventricles. *Circulation research*, 23(2):203–211, 1968.

[79] A. Palit, P. Franciosa, S. K. Bhudia, T. N. Arvanitis, G. A. Turley, and M. A. Williams. Passive diastolic modelling of human ventricles: Effects of base movement and geometrical heterogeneity. *Journal of Biomechanics*, 52:95–105, Feb. 2017.

[80] Y. C. Pao, E. L. Ritman, and E. H. Wood. Finite-element analysis of left ventricular myocardial stresses. *Journal of Biomechanics*, 7(6):469–477, Nov. 1974.

[81] K. Perktold, K. Gruber, T. Kenner, and H. Florian. Calculation of pulsatile flow and particle paths in an aneurysm-model. *Basic Research in Cardiology*, 79(3):253–261, May 1984.

[82] M. J. Powell. The BOBYQA algorithm for bound constrained optimization without derivatives, Department of Applied Mathematics and Theoretical Physics. *Technical report*, 2009.

[83] S. Rich, E. Kaufmann, and P. S. Levy. The Effect of High Doses of Calcium-Channel Blockers on Survival in Primary Pulmonary Hypertension. *New England Journal of*

Medicine, 327(2):76–81, July 1992.

[84] S. Rossi, R. Ruiz-Baier, L. F. Pavarino, and A. Quarteroni. Orthotropic active strain models for the numerical simulation of cardiac biomechanics. *International Journal for Numerical Methods in Biomedical Engineering*, 28(6-7):761–788, 2012.

[85] L. J. Rubin. Therapy of Pulmonary Hypertension. *American Journal of Respiratory and Critical Care Medicine*, 166(10):1308–1309, Nov. 2002.

[86] K. L. Sack, N. H. Davies, J. M. Guccione, and T. Franz. Personalised computational cardiology: Patient-specific modelling in cardiac mechanics and biomaterial injection therapies for myocardial infarction. *Heart Failure Reviews*, 21(6):815–826, Nov. 2016.

[87] H. Schmid, M. P. Nash, A. A. Young, and P. J. Hunter. Myocardial Material Parameter Estimation—A Comparative Study for Simple Shear. *Journal of Biomechanical Engineering*, 128(5):742–750, Mar. 2006.

[88] P. Seegerer, T. Mansi, M.-P. Jolly, D. Neumann, B. Georgescu, A. Kamen, E. Kayvanpour, A. Amr, F. Sedaghat-Hamedani, and J. Haas. Estimation of regional electrical properties of the heart from 12-lead ECG and images. *International Workshop on Statistical Atlases and Computational Models of the Heart*, pages 204–212, 2014.

[89] M. Sellier. An iterative method for the inverse elasto-static problem. *Journal of Fluids and Structures*, 27(8):1461–1470, Nov. 2011.

[90] J. C. Simo and R. L. Taylor. Quasi-incompressible finite elasticity in principal stretches. continuum basis and numerical algorithms. *Computer Methods in Applied Mechanics and Engineering*, 85(3):273–310, Feb. 1991.

[91] O. Sitbon, M. Humbert, V. Ioos, X. Jais, F. Parent, and G. Garcia. Who benefits from long-term calcium-channel blocker therapy in primary pulmonary hypertension. *Am J Respir Crit Care Med*, 167:A440, 2003.

[92] Streeter Daniel D., Spotnitz Henry M., Patel Dali P., Ross John, and Sonnenblick Edmund H. Fiber Orientation in the Canine Left Ventricle during Diastole and Systole. *Circulation Research*, 24(3):339–347, Mar. 1969.

[93] K. Sun, N. Stander, C.-S. Jhun, Z. Zhang, T. Suzuki, G.-Y. Wang, M. Saeed, A. W. Wallace, E. E. Tseng, A. J. Baker, D. Saloner, D. R. Einstein, M. B. Ratcliffe, and J. M. Guccione. A Computationally Efficient Formal Optimization of Regional Myocardial Contractility in a Sheep With Left Ventricular Aneurysm. *Journal of Biomechanical Engineering*, 131(11):111001–111001–10, Oct. 2009.

[94] J. Sundnes, S. Wall, H. Osnes, T. Thorvaldsen, and A. D. McCulloch. Improved discretisation and linearisation of active tension in strongly coupled cardiac electro-mechanics simulations. *Computer Methods in Biomechanics and Biomedical Engineering*, 17(6):604–615, Apr. 2014.

[95] L. A. Taber and R. Perucchio. Modeling Heart Development. *Journal of elasticity and*

the physical science of solids, 61(1):165–197, July 2000.

[96] R. J. Tallarida, B. F. Rusy, and M. H. Loughnane. Left ventricular wall acceleration and the law of Laplace. *Cardiovascular Research*, 4(2):217–223, Apr. 1970.

[97] B. T. Tang, C. P. Cheng, M. T. Draney, N. M. Wilson, P. S. Tsao, R. J. Herfkens, and C. A. Taylor. Abdominal aortic hemodynamics in young healthy adults at rest and during lower limb exercise: Quantification using image-based computer modeling. *American Journal of Physiology-Heart and Circulatory Physiology*, 291(2):H668–H676, Aug. 2006.

[98] D. Tang, P. J. del Nido, C. Yang, H. Zuo, X. Huang, R. H. Rathod, V. Gooty, A. Tang, Z. Wu, K. L. Billiar, and T. Geva. Patient-Specific MRI-Based Right Ventricle Models Using Different Zero-Load Diastole and Systole Geometries for Better Cardiac Stress and Strain Calculations and Pulmonary Valve Replacement Surgical Outcome Predictions. *PLOS ONE*, 11(9):e0162986, Sept. 2016.

[99] C. Taylor and C. Figueroa. Patient-Specific Modeling of Cardiovascular Mechanics. *Annual Review of Biomedical Engineering*, 11(1):109–134, 2009.

[100] N. Toussaint, C. T. Stoeck, T. Schaeffter, S. Kozerke, M. Sermesant, and P. G. Batchelor. In vivo human cardiac fibre architecture estimation using shape-based diffusion tensor processing. *Medical Image Analysis*, 17(8):1243–1255, Dec. 2013.

[101] T. Usyk, R. Mazhari, and A. McCulloch. Effect of Laminar Orthotropic Myofiber Architecture on Regional Stress and Strain in the Canine Left Ventricle. *Journal of elasticity and the physical science of solids*, 61(1):143–164, July 2000.

[102] J. L. Vachiery, S. Brimioulle, V. Crasset, and R. Naeije. False-positive diagnosis of pulmonary hypertension by Doppler echocardiography. *European Respiratory Journal*, 12(6):1476–1478, Dec. 1998.

[103] G. Venter. Review of Optimization Techniques. In *Encyclopedia of Aerospace Engineering*. American Cancer Society, 2010.

[104] von Deuster Constantin, Sammut Eva, Asner Liya, Nordsletten David, Lamata Pablo, Stoeck Christian T., Kozerke Sebastian, and Razavi Reza. Studying Dynamic Myofiber Aggregate Reorientation in Dilated Cardiomyopathy Using In Vivo Magnetic Resonance Diffusion Tensor Imaging. *Circulation: Cardiovascular Imaging*, 9(10):e005018, Oct. 2016.

[105] D. A. Vorp. Biomechanics of abdominal aortic aneurysm. *Journal of Biomechanics*, 40(9):1887–1902, Jan. 2007.

[106] J. C. Walker, M. B. Ratcliffe, P. Zhang, A. W. Wallace, B. Fata, E. W. Hsu, D. Saloner, and J. M. Guccione. MRI-based finite-element analysis of left ventricular aneurysm. *American Journal of Physiology-Heart and Circulatory Physiology*, 289(2):H692–H700, Aug. 2005.

[107] H. M. Wang, H. Gao, X. Y. Luo, C. Berry, B. E. Griffith, R. W. Ogden, and T. J. Wang. Structure-based finite strain modelling of the human left ventricle in diastole. *International Journal for Numerical Methods in Biomedical Engineering*, 29(1):83–103, Jan. 2013.

[108] V. Y. Wang, H. I. Lam, D. B. Ennis, B. R. Cowan, A. A. Young, and M. P. Nash. Modelling passive diastolic mechanics with quantitative MRI of cardiac structure and function. *Medical Image Analysis*, 13(5):773–784, Oct. 2009.

[109] V. Y. Wang, H. I. Lam, D. B. Ennis, B. R. Cowan, A. A. Young, and M. P. Nash. Modelling passive diastolic mechanics with quantitative MRI of cardiac structure and function. *Medical Image Analysis*, 13(5):773–784, Oct. 2009.

[110] A. Y. K. Wong and P. M. Rautaharju. Stress distribution within the left ventricular wall approximated as a thick ellipsoidal shell. *American Heart Journal*, 75(5):649–662, May 1968.

[111] J. Wong and E. Kuhl. Generating fibre orientation maps in human heart models using Poisson interpolation. *Computer Methods in Biomechanics and Biomedical Engineering*, 17(11):1217–1226, Aug. 2014.

[112] R. H. Woods. A few applications of a physical theorem to membranes in the human body in a state of tension. *Transactions of the Royal Academy of Medicine in Ireland*, 10(1):417, Dec. 1892.

[113] C. Xi, C. Latnie, X. Zhao, J. L. Tan, S. T. Wall, M. Genet, L. Zhong, and L. C. Lee. Patient-Specific Computational Analysis of Ventricular Mechanics in Pulmonary Arterial Hypertension. *Journal of Biomechanical Engineering*, 138(11):111001–111001–9, Oct. 2016.

[114] J. Xi, P. Lamata, S. Niederer, S. Land, W. Shi, X. Zhuang, S. Ourselin, S. G. Duckett, A. K. Shetty, C. A. Rinaldi, D. Rueckert, R. Razavi, and N. P. Smith. The estimation of patient-specific cardiac diastolic functions from clinical measurements. *Medical Image Analysis*, 17(2):133–146, Feb. 2013.

[115] F. C. Yin, C. C. Chan, and R. M. Judd. Compressibility of perfused passive myocardium. *American Journal of Physiology-Heart and Circulatory Physiology*, 271(5):H1864–H1870, Nov. 1996.

[116] H. Zou, C. Xi, X. Zhao, A. S. Koh, F. Gao, Y. Su, R.-S. Tan, J. Allen, L. C. Lee, M. Genet, and L. Zhong. Quantification of Biventricular Strains in Heart Failure With Preserved Ejection Fraction Patient Using Hyperelastic Warping Method. *Frontiers in Physiology*, 9, Sept. 2018.

APPENDIX A

Unidirectional Contraction of a Tissue Cube

To show that the active stress and active strain approaches to modelling active contraction of the myocardium can produce similar stress predictions in a simplified setting, we considered the case of a tissue cube with uniform fibre orientation aligned with one of the principal axes; in this case, the x-axis. What follows is based on notes provided by Joakim Sundnes. The cube undergoes unidirectional contraction against a linear spring force which results in a uniform deformation state with a diagonal deformation gradient. Assuming tissue incompressibility, we can write the deformation gradient as $\mathbf{F} = diag(\lambda, \lambda^{-1/2}, \lambda^{-1/2})$, with λ being the stretch in the fibre direction. First, we consider the active strain model, and decompose $\mathbf{F}$ as

$$\mathbf{F} = \mathbf{F}_e\mathbf{F}_a.$$

with $\mathbf{F}_a = diag((1-\gamma), (1-\gamma)^{-1/2}, (1-\gamma)^{-1/2})$, where γ is a parameter describing active muscle shortening (active strain parameter). The elastic component of the deformation gradient, $\mathbf{F}_e$, is given by

$$\mathbf{F}_e = \mathbf{F}\mathbf{F}_a^{-1} = \begin{pmatrix} \lambda(1-\gamma)^{-1} & 0 & 0 \\ 0 & \lambda^{-1/2}(1-\gamma)^{1/2} & 0 \\ 0 & 0 & \lambda^{-1/2}(1-\gamma)^{1/2} \end{pmatrix}.$$

A corresponding decomposition of the right Cauchy-Green tensor, $\mathbf{C}$ gives

$$\mathbf{C} = \mathbf{F}^T\mathbf{F} = (\mathbf{F}_e\mathbf{F}_a)^T(\mathbf{F}_e\mathbf{F}_a) = \mathbf{F}_a^T\mathbf{F}_e^T\mathbf{F}_e\mathbf{F}_a = \mathbf{F}_a^T\mathbf{C}_e\mathbf{F}_a,$$

and with the uniform deformation state considered here, $\mathbf{C}_e$ is diagonal with components

$$C_{e,11} = \lambda^2(1-\gamma)^{-2},$$
$$C_{e,22} = C_{e,33} = \lambda^{-1}(1-\gamma).$$

Based on the chosen strain-energy function (Equation 3.30 in Section 3.3.1), we have the Cauchy stress as

$$\sigma = ae^{b(I_1-3)}\mathbf{F}\mathbf{F}^T + 2a_f(I_{4f}-1)e^{b_f(I_{4f}-1)^2}\mathbf{F}(\mathbf{f}_0 \otimes \mathbf{f}_0)\mathbf{F}^T - p\mathbf{I}. \tag{1}$$

where I_1, I_{4f} are invariants of $\mathbf{C}_e$, given by

$$I_1 = \mathrm{tr}(\mathbf{C}_e), \quad I_{4f} = \mathbf{f}_0 \cdot (\mathbf{C}_e\mathbf{f}_0),$$

with $\mathbf{f}_0$ being a unit vector aligned with the fiber orientation. For the deformation state considered here, the invariants are given as

$$I_1 = \lambda^2(1-\gamma)^{-2} + 2\lambda^{-1}(1-\gamma), \tag{2}$$
$$I_{4f} = \lambda^2(1-\gamma)^{-2}, \tag{3}$$

and the resulting Cauchy stress tensor is diagonal with the following components:

$$\sigma_{11} = ae^{b(I_1-3)}\lambda^2 + 2a_f(I_{4f}-1)e^{b_f(I_4f-1)^2}\lambda^2 - p, \tag{4}$$
$$\sigma_{22} = \sigma_{33} = ae^{b(I_1-3)}\lambda^{-1} - p. \tag{5}$$

Since the cube is unloaded and therefore stress free in the transverse directions, (5) gives

$$p = ae^{b(I_1-3)}\lambda^{-1},$$

and we insert this into (4) to get

$$\sigma_{11} = ae^{b(I_1-3)}(\lambda^2 - \lambda^{-1}) + 2a_f(I_{4f}-1)e^{b_f(I_4f-1)^2}\lambda^2. \tag{6}$$

This gives a simple relation between active strain parameter γ, fibre shortening λ and fibre stress σ_{11}.

On the other hand, considering the active stress model, the deformation gradient and thus the right Cauchy-Green tensor are not decomposed into an elastic and active

part. Hence the right Cauchy-Green tensor is given by

$$\mathbf{C} = \mathbf{F}^T\mathbf{F},$$

which is a diagonal tensor with components

$$C_{11} = \lambda^2,$$
$$C_{22} = C_{33} = \lambda^{-1}.$$

Thus the invariants I_1, I_{4f} read as

$$I_1 = \lambda^2 + 2\lambda^{-1}, \tag{7}$$
$$I_{4f} = \lambda^2. \tag{8}$$

The Cauchy stress expression in (6) makes up the passive component in the active stress model, and the active component of the total stress takes the form

$$\sigma_a = \mathbf{T}_a\mathbf{F}(\mathbf{f}_0 \otimes \mathbf{f}_0)\mathbf{F}^T,$$

where $\mathbf{T}_a$ is the active stress parameter. This expression simplifies to

$$\sigma_a = \mathbf{T}_a\lambda^2. \tag{9}$$

Thus, by the active stress model, we add (6) and (9), to get the total Cauchy stress as

$$\sigma_{11} = ae^{b(I_1-3)}(\lambda^2 - \lambda^{-1}) + 2a_f(I_{4f} - 1)e^{b_f(I_4f-1)^2}\lambda^2 + \mathbf{T}_a\lambda^2. \tag{10}$$

which gives a simple relation between the active stress parameter $\mathbf{T}_a$, fibre shortening λ and fibre stress σ_{11}. We used Equations (6) and (10) to predict stress on the tissue cube and compared the stress results to see if both approaches produce identical stress predictions. As stated earlier, the tissue cube contracts against a linear spring force. The resulting balance equation is

$$\sigma_{tissue} + \sigma_{series} = 0,$$

where σ_{tissue} is given by Equation (6) for the active strain model or Equation (10) for

the active stress model. σ_{series} is the linear spring force given as

$$\sigma_{series} = k_{se}(\lambda - \lambda_0).$$

Here, k_{se} is the spring stiffness. We have chosen $k_{se} = 50$, which gives reasonable contraction dynamics for the tissue. We used the fitted active strain parameter γ, and active stress parameter $\mathbf{T}_a$ for one of the subjects used in this thesis as input. The material parameters a, b, a_f, b_f were selected based on optimized values for the subject. The python code for performing the computations is attached below:

```
import numpy as np
import os
import matplotlib.pyplot as plt
from scipy.optimize import fsolve
import seaborn as sns

sns.set()

"""Cauchy stress based on active strain formulation"""

def active_strain(lmbda,gamma):

    a, a_f, b, b_f = 1.78454663458,2.582,5.0,5.0

    l, g = lmbda, gamma

    I4f = l**2/(1-g)**2

    I1 = I4f+2*(1-g)/l

    f_iso = a * np.exp(b*(I1-3))*(l**2-1/l)

    f_fib = 2*a_f*(I4f-1)*np.exp(b_f*(I4f-1)**2)*l**2

    force_ATSR = (f_iso+f_fib)

    return force_ATSR
```

```
"""Cauchy stress based on active stress formulation"""

def active_stress(lmbda,sigma):

    a, a_f, b, b_f = 1.78454663458,2.582,5.0,5.0

    l = lmbda

    I4f = l**2

    I1 = I4f + 2*(1/l)

    f_iso = a * np.exp(b*(I1-3))*(l**2-1/l)

    f_fib = 2*a_f*(I4f-1)*np.exp(b_f*(I4f-1)**2)*l**2

    force_passive = (f_iso+f_fib)

    force_active = sigma*(l**2)

    force = force_passive + force_active

    return force

"""force balance based on active stress formulation"""

def force_balance(lmbda,sigma,lmbda_0):

    k_se = 50.0

    f_serial = k_se*(lmbda-lmbda_0)

    return f_serial + active_stress(lmbda,sigma)


"""force balance based on active strain formulation"""
```

```
def force_balance_ATSR(lmbda,gamma,lmbda_0):

    k_se = 50.0

    f_serial = k_se*(lmbda-lmbda_0)

    return f_serial + active_strain(lmbda,gamma)

"""solve for deformation and stress based on active stress formulation"""
data = np.loadtxt('.//data/data/gamma_MR016_active_stress.csv',
                  skiprows=1,delimiter =',')

sigma = data[:,0]*0.035

force = np.zeros_like(sigma)

l0 = 0.9

lmbda = []

force = []

for t in sigma:

    l = fsolve(force_balance,l0,args = (t,l0))

    lmbda.append(l)

    force.append(active_stress(l,t))

"""solve for deformation and stress based on active strain formulation"""
data_ATSR = np.loadtxt('.//data/data/gamma_MR016_active_strain.csv',
                       skiprows=1,delimiter =',')

gamma = data_ATSR[:,0]
```

```
force_ATSR = np.zeros_like(gamma)

l1 = 0.9

lmbda_ATSR = []

force_ATSR = []

for g in gamma:

    ll = fsolve(force_balance_ATSR,l1,args = (g,l1))

    lmbda_ATSR.append(ll)

    force_ATSR.append(active_strain(ll,g))

"""plot active stress parameter"""

plt.figure(1)

plt.title('Active stress $\sigma$, MR016')

plt.plot(sigma)

"""plot active strain parameter"""

plt.figure(2)

plt.title('Active strain $\gamma$, MR016')

plt.plot(gamma)

"""
plot deformation and 1D stress comparison
between active stress and active strain formulations
"""
```

```
fig, (ax1, ax2) = plt.subplots(1, 2, figsize=(6,8))

line_labels = ['active stress', 'active strain']

l1 = ax1.plot(lmbda, 'o-', linewidth=2.5)[0]
l2 = ax1.plot(lmbda_ATSR, 'o-', linewidth=2.5)[0]
l3 = ax2.plot(force, 'o-', linewidth=2.5)[0]
l4 = ax2.plot(force_ATSR, 'o-', linewidth=2.5)[0]

axes = [ax1, ax2]

for i in axes:
    plt.setp(i.get_xticklabels(), fontsize=18)
    plt.setp(i.get_yticklabels(), fontsize=18)
    i.xaxis.labelpad = 10
    i.yaxis.labelpad = 15

fig.legend([l3, l4],
           labels=line_labels,
           loc='center right',
           borderaxespad=0.7,
           title='',
           fontsize=24,
           frameon=False
          )

ax1.set_xlabel('Time point\n', fontsize=22)
ax1.set_ylabel('Deformation', fontsize=22)
ax2.set_xlabel('Time point\n', fontsize=22)
ax2.set_ylabel('Cauchy stress (kPa)', fontsize=22)
plt.subplots_adjust(right=0.80, wspace=0.3)

plt.show()
```